Identifying the unique ground motion signatures of supershear earthquakes: Theory and experiments

M. Mello [a,*], H.S. Bhat [a,b], A.J. Rosakis [a], H. Kanamori [a]

[a] Graduate Aerospace Laboratories, California Institute of Technology, USA
[b] Department of Earth Sciences, University of Southern California, USA

ABSTRACT

The near field ground motion signatures associated with sub-Rayleigh and supershear ruptures are investigated using the laboratory earthquake experiment originally developed by Rosakis and coworkers (Xia et al., 2004, 2005a; Lu et al., 2007; Rosakis et al., 2007). Heterodyne laser interferometers enable continuous, high bandwidth measurements of fault-normal (FN) and fault-parallel (FP) particle velocity "ground motion" records at discrete locations on the surface of a Homalite test specimen as a sub-Rayleigh or a supershear rupture sweeps along the frictional fault. Photoelastic interference fringes, acquired using high-speed digital photography, provide a synchronized, spatially resolved, whole field view of the advancing rupture tip and surrounding maximum shear stress field. Experimental results confirm that near field ground motion records associated with the passage of a sub-Rayleigh rupture are characterized by a FN velocity swing which dominates over the FP velocity swing. The situation is shown to reverse in the supershear rupture speed regime whereby the motion along the shear Mach front is characterized by a FP particle velocity swing which dominates over the FN velocity swing.

Additional distinguishing particle velocity signatures, consistent with theoretical and numerical predictions, and repeatedly observed in experimental records are (1) a pronounced peak in the FP velocity record, induced by the leading dilatational field, which sweeps the measurement station just prior to the arrival of the shear Mach front, and (2) a pronounced velocity swing in the FN record associated with the arrival of a "trailing Rayleigh disturbance", which sweeps the measurement station following passage of the shear Mach front. Each of these features are addressed in detail. We conclude by reexamining the 2002, M_w7.9 Denali fault earthquake and the remarkable set of ground motion records obtained at Pump Station 10 (PS10), located approximately 85 km east of the epicenter and 3 km north of the fault along the Alaska Pipeline. Motivated by the analysis and thorough interpretation of these records by Dunham and Archuleta (2004, 2005), we attempt to replicate the Denali ground motion signatures using a laboratory earthquake experiment. The experiments feature a left (west) to right (east) propagating right lateral rupture within the Homalite test specimen with particle velocity data collected at a near-field station situated just above (north of) the fault, (on the compressional quadrant) in order to simulate the PS10 scenario. Both sub-Rayleigh and supershear laboratory earthquake experiments are conducted using the "Denali PS10" configuration in order to compare and contrast the resulting particle velocity signatures. Results from the supershear experiment capture the prominent FN and FP ground motion signatures and corresponding sense of particle motion revealed in the PS10 ground motion records. Most notably, the particle velocity records feature a dominant FP component coinciding with the arrival of the shear Mach front, followed by a pronounced velocity swing in the FN component coinciding with the passage of a trailing Rayleigh disturbance, as independently confirmed by the presence of these features and their noted arrival times in the synchronized photoelastic image sequence.

© 2010 Elsevier B.V. All rights reserved.

1. Introduction

A natural earthquake is classified as supershear if it is surmised, generally with the aid of seismic inversions, that the primary rupture spent some portion of its history in the rupture speed regime $C_s \leq V_r \leq C_p$, where V_r represents the rupture speed, and C_s, C_p represent the crustal shear (S) and pressure (P) wave speeds, respectively. Rupture speed stability analyses have been performed within the context of either self-similar crack growth (Andrews, 1976; Burridge et al., 1979; Broberg, 1989) or by using steady-state, cohesive shear strength models (Rosakis, 2002; Samudrala et al., 2002a,b; Dunham and Archuleta, 2004, 2005) under uniform

background stress and fault strength conditions. It is well established that once a rupture front has transitioned into the supershear domain it will tend to favor a stable rupture speed regime $V_0 < V_r \leq C_p$ with $V_r \rightarrow C_p$, given a sufficient rupture propagation distance in the case of self-similar growth. The lower bound V_0 of the stable regime is a function of the fault strength and may also depend upon other system parameters such as rate of velocity weakening and background stress. The minimum value that V_0 can assume, in the case of infinite fault strength, is $V_0 = \sqrt{2}C_s$ in which case the maximum extent of the stable rupture speed regime becomes $\sqrt{2}C_s < V_r \leq C_p$. The rupture speed domain $C_s \leq V_r < V_0$, is consequently regarded as an unstable rupture speed regime. Earthquakes are otherwise generally classified as sub-Rayleigh, exhibiting a rupture speed bounded by $V_r \leq C_R$ with the rupture speed tending to approach the Rayleigh wave speed C_R (Broberg, 1999; Rosakis, 2002). The rupture speed regime $C_R < V_r < C_s$ is forbidden since a rupture in this speed regime would otherwise become a source rather than a sink of fracture energy (Freund, 1979; Broberg, 1989; Rosakis, 2002). The superposition of shear wavelets emitted by a steady state, supershear rupture front leads to the formation of a shear Mach front, which stems from the advancing rupture tip and envelopes the surrounding medium along either side of the fault. Considerable insight into the formation of a shear Mach front and the nature of the resulting displacement field along the front is gained by recalling the solution to the far field radiation pattern for the transverse component of displacement due to a right lateral shear dislocation, also commonly referred to as the double-couple solution in an infinite homogeneous medium (Aki and Richards, 2002).

The series of diagrams depicted in Fig. 1 graphically demonstrate the formation of sub-Rayleigh rupture and shear Mach fronts by the superposition of S-wave fronts emitted by a steady state right-lateral rupture. Fig. 1a shows how the displacement field vectors lying tangent to the arc of a circular S-wave front are oriented clockwise along the upper portion of the wave front corresponding to $\pi/4 < \phi \leq \pi/2$. The displacement field vectors continuously decrease in magnitude along the S-wave front from a maximum value at $\phi = \pi/2$ until disappearing at the nodal point corresponding to $\phi = \pi/4$. The displacement field vectors along the upper quadrant are thus characterized by a dominant FP component. The nodal point at $\phi = \pi/4$ also marks a reversal point in the displacement field. Displacement field vectors lying tangent to the lower portion of the circular S-wave front are now oriented counterclockwise as shown, featuring a continuous increase in magnitude starting from the nodal point at $\phi = \pi/4$ until a maximum value is attained at $\phi = 0$. Note that

the displacement field vectors along the lower sector are now characterized by a dominant FN component.

Fig. 1b depicts a steady state, right-lateral shear dislocation emitting S-wave fronts as it propagates from left to right along the horizontal axis. When propagating at a speed $V_r \leq C_R$, (i.e. sub-Rayleigh rupture speed regime), the radiated S-wave fronts will tend to pile up to form a locally concentrated field just ahead of the advancing rupture as shown. The resulting velocity field surrounding a sub-Rayleigh rupture, particularly in the region situated ahead of the rupture tip, is thus characterized by a dominant FN component, corresponding to the dominant component of motion along the contributing S-wave fronts.

The lower two diagrams in Fig. 1 graphically depict how the circular S-wave fronts emitted by a steady state supershear rupture combine to form an inclined Mach front, which is tangent to the continuum of shear wavelets as shown. Any line drawn normal to the Mach front will necessarily pass through the center of a contributing circular S-wave front that was emitted by the rupture at an earlier time. The acute angle ϕ measured between the normal the Mach front and the fault plane, is naturally the same for all of the S-waves that combine to form a given Mach front. The resulting displacement field $\vec{u}_s$ is thus oriented parallel to the shear Mach front as shown.

Note that since the angle $\phi = \pi/4$ corresponds to a nodal point along a S-wave front, it follows that the Mach angle $\theta = \pi/4$ represents a natural boundary in the supershear regime whereby $\vec{u}_s$ is directed upward along the front for $\theta > \pi/4$ as depicted in Fig. 1c (i.e. $\phi < \pi/4$), and otherwise directed downward along the shear Mach front for $\theta < \pi/4$ as depicted in Fig. 1d (i.e. $\phi > \pi/4$).

The propagation direction of the shear Mach front is defined by a wave vector $\vec{k}$, which is oriented at an angle ϕ with respect to the fault plane as shown, while the resulting Mach cone half-angle, measured with respect to the fault plane, is given by the familiar relation

$$\theta = \sin^{-1}(C_s / V_r). \tag{1}$$

where $\theta = \pi/2 - \phi$ (see Section 2.2).

Application of Eq. (1) reveals that $\theta = \pi/4$ corresponds to the unique rupture speed $V_r = \sqrt{2}C_s$. Consequently, $|\vec{u}_s| \rightarrow 0$ as $V_r \rightarrow \sqrt{2}C_s$ since all of the contributing shear wavelets are nodal at the point of tangency to the Mach front when $\phi = \pi/4$. The complete disappearance of the shear Mach front at this unique rupture speed and the resulting no-radiation condition is addressed in greater detail in a later section.
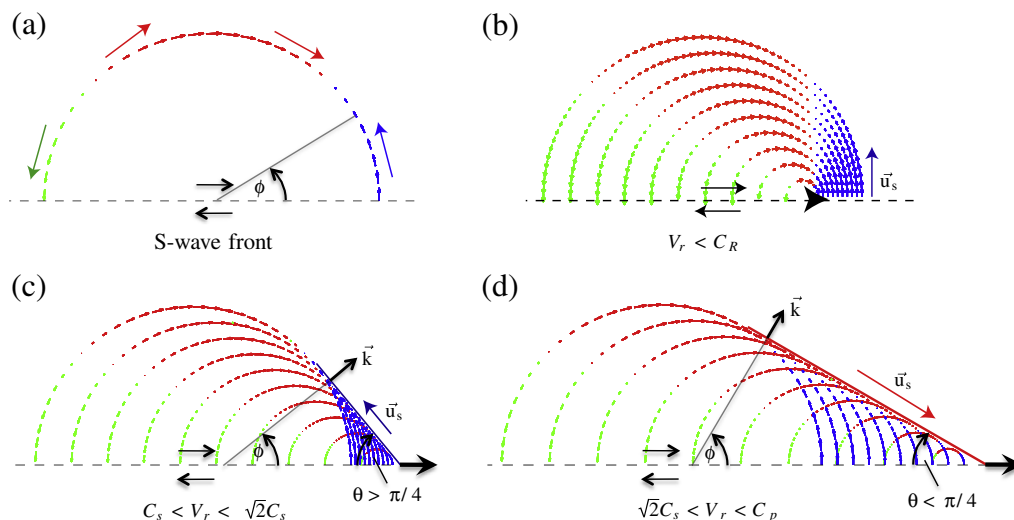

Fig. 1. Formation of sub-Rayleigh rupture and shear Mach fronts by the superposition of shear wavelets emitted by a steady-state shear dislocation.

Continued application of Eq. (1) reveals that the Mach angle domain $\pi/4 < \theta \leq \pi/2$ corresponds to the rupture speed domain $C_s \leq V_r < \sqrt{2}C_s$ while $\sin^{-1}(C_s/C_p) \leq \theta < \pi/4$ corresponds to the maximum stable rupture speed regime $\sqrt{2}C_s < V_r \leq C_p$. Special cases of interest that set the lower bound $\theta_{min} = \sin^{-1}(C_s/C_p)$ are (1) $C_p = \sqrt{3}C_s$, often to be a good approximation for crustal rock, whereby $\sin^{-1}(1/\sqrt{3}) \leq \theta < \pi/4$, and (2) $C_p \approx 2C_s$, applicable to H-100 test specimens used in laboratory earthquake experiments, whereby $\sin^{-1}(1/2) \leq \theta < \pi/4$. Near field locations, which are swept by a shear Mach front are subject to unique forms of ground motion, induced by various aspects of the radiated fields, which necessarily differ from classical sub-Rayleigh ground motion. The nature of supershear ground motion and any features that distinguish it from sub-Rayleigh ground motion form the basis of the experimental investigation contained in this article. Ground motion signatures associated with sub-Rayleigh and supershear ruptures are investigated using the Laboratory Earthquake Experiment developed by Rosakis and co-workers (Xia et al., 2004; Lu et al., 2007, 2010; Rosakis et al., 2007). Heterodyne laser interferometers (Lykotrafitis et al., 2006a) enable continuous, high bandwidth measurements of FN and FP particle velocity "ground motion" records at fixed locations on the surface of a Homalite ™(H-100) test specimen as a sub-Rayleigh or supershear rupture sweeps along the frictional fault. Photoelastic interference fringes, acquired using high-speed digital photography, provide a synchronized, spatially resolved, whole field view of the advancing rupture tip and surrounding maximum shear stress field. Fig. 2 captures the essence of the experimental strategy adopted in the current investigation. A photoelastic image reveals a supershear rupture and a associated shear Mach fronts which sweep the material to either side of the specimen fault. One of the Mach fronts is seen just crossing a particle velocity measurement station on the surface of the specimen. The red arrows highlight how a pair of laser beams are directed at nearly grazing incidence to the specimen surface and brought to focus at the lower right hand corner of a measurement station. Simultaneous FN and FP particle velocity records acquired at this location are analogous to ground motion measurements recorded by an accelerometer station situated in the immediate neighborhood of an active fault. Additional features such as a leading dilatational field lobe surrounding the rupture tip and the trailing secondary slip pulse in the wake of the shear Mach cone are also revealed in the image. A more precise description of these features along with a detailed discussion of the experimental arrangement and optical diagnostics are addressed in later sections. Results obtained through experiments replicate and validate numerous supershear ground motion features pre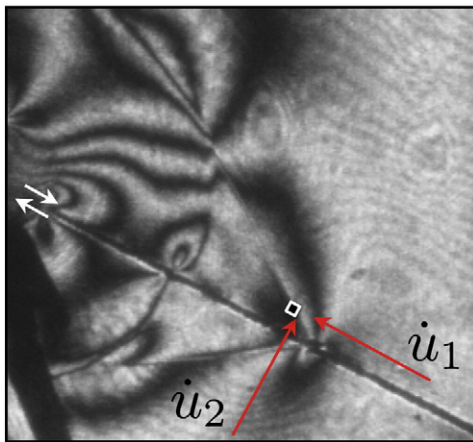dicted by both theory and numerical analysis. Knowledge gained through these investigations not only validates and ranks the fidelity of various theoretical and numerical predictions but can also provide an improved understanding of frictional faulting processes. Laboratory earthquake experiments also serve to emphasize the utility and potential payoff of acquiring ground motion measurements in the local vicinity of active faults on the surface of the Earth.

There have been at least seven natural earthquakes, chronologically listed in Table 1, that have been classified as, or at least conjectured to have been supershear events (Archuleta, 1984; Bouchon et al., 2001, 2002; Bouchon and Vallee, 2003; Bouin et al., 2004; Dunham and Archuleta, 2004; Ellsworth et al., 2004; Robinson et al., 2006; Song et al., 2008; Ellsworth and Chiaraluce, 2009). Most of these large magnitude events occurred in long and relatively straight fault segments and at least two (M_w7.8 Kunlunshan, Tibet and M_w7.9 Denali, Alaska) featured a well documented transition from sub-Rayleigh to supershear speeds. Some of the necessary conditions, which increase the likelihood for a fault segment to host a supershear earthquake rupture have been studied by Robinson et al. (2006), Das (2007).

In all events listed in Table 1, finite fault inversion techniques, constrained by geodetic and/or seismic data, were applied to estimate the rupture velocity history so as to infer where and when along the fault the rupture may have transitioned into the supershear domain. In some of these cases there is compelling field data to support this assertion. Generally speaking however, there is an overall scarcity of reliable near field ground motion records, thus placing a heavy reliance upon the use of seismic inversion techniques in order to conclude whether most of the events listed in Table 1 were supershear earthquakes. A notable exception in the list is the 2002 M_w7.9 Denali, Alaska earthquake, in which case a unique set of near field ground motion records signal the passage of a supershear rupture followed by a secondary slip pulse (Dunham and Archuleta, 2004, 2005). Motivated by the unique features contained in these ground motion records and by a dynamic rupture simulation of the event conducted by Dunham and Archuleta (2004, 2005), a series of laboratory earthquake experiments were conducted in an attempt to replicate the Denali near-source ground motion signatures using a model test specimen. Particle velocity records bearing a striking similarity to the Denail ground motion records are presented and discussed.

2. 2D steady-state rupture theory: sub-Rayleigh vs. supershear ruptures

Recent theoretical and numerical investigations of supershear ruptures in 2D (Dunham and Archuleta, 2005; Bhat et al., 2007), and in 3D (Dunham and Bhat, 2008) show that ground motion due to the passage of the Mach front is virtually unattenuated at large distances from the fault. This conclusion is qualitatively consistent with high speed photoelastic images of supershear ruptures, which extend out to large distances from the rupture tip (Rosakis et al., 1999; Rosakis, 2002; Lu et al., 2007). In their numerical 2D steady-state supershear slip pulse model, Dunham and Archuleta (2005), showed that the

Fig. 2. Supershear rupture with shear Mach front, as revealed by photoelastic interference fringes, shown crossing a particle velocity measurement station during a laboratory earthquake experiment.

Table 1
Natural earthquakes inferred to have been supershear events.

Year	Location	M_w
18 April 1906	San Fransisco, CA	7.9
15 October 1979	Imperial Valley, CA	6.5
17 August 1999	Izmit, Turkey	7.6
12 November 1999	Duzce, Turkey	7.2
14 November 2001	Kunlunshan, Tibet	7.8
3 November 2002	Denali, Alaska	7.9
6 April 2009	L'Aquila, Abruzzo, Italy	6.3

supershear rupture S-wave spectrum is transported out to infinity along Mach line characteristics emanating exclusively from within the slip zone. Supershear ground motion records gathered far from the fault should thus contain detailed information about the frictional faulting process in stark contrast to the sub-Rayleigh ground motion records, which suffer rapid attenuation with increased off-fault distance and reveal little information about the rupture source spectrum (Dunham and Archuleta, 2005).

The Fourier transform based spectral representation of the radiated wave fields arising from a steady-state sub-Rayleigh rupture pulse, which is presented here augments these earlier studies. The analysis clearly reveals how an on-fault rupture pulse source spectrum is rapidly stripped of its high frequency content with increased off-fault distance, thus leaving little chance of extracting detailed information about the breakdown zone from off-fault ground motion records. A similar analysis applied to a 2D supershear rupture pulse is also presented below, which reveals how the S-wave source spectrum remains fully preserved out to infinity, implying that off-fault ground motion records contain detailed information about the frictional faulting process.

2.1. Fourier analysis of sub-shear rupture fields

Elastic wave fields may be separated into dilatational (irrotational) and shear (rotational) parts, each governed by the wave equation and an appropriate wave speed. For the sake of clarification, we note that dilatational waves, primary waves, pressure (P) waves are all synonymous in the context of this discussion. Adopting the Poisson representation, the displacement field may be expressed as

$$\vec{u} = \vec{u}^p + \vec{u}^s \tag{2}$$

where $\vec{u}^p$ and $\vec{u}^s$ represent the dilatational (P) and shear (S) displacement fields, respectively. Each displacement field component is in turn governed by the wave equation (Freund, 1990) provided that

$$\nabla \times \vec{u}^p = 0 \tag{3}$$

$$\nabla \cdot \vec{u}^s = 0 \tag{4}$$

Consider a 2D rupture propagating along a frictional fault coinciding with the x-axis of a Cartesian coordinate system. By imposing the steady-state assumption and taking the origin of a new coordinate system (ξ_1, ξ_2) to coincide with the rupture front, the governing wave equation expressions become two-dimensional in $\xi_1 = x - V_r t$ and $\xi_2 = y$ under a Galilean coordinate transformation. A general field quantity $f(\xi_1, \xi_2)$ (which may represent any stress or particle velocity field component), associated with a rupture speed V_r, may therefore be expressed as

$$f(\xi_1, \xi_2) = f^p(\xi_1, \xi_2) + f^s(\xi_1, \xi_2) \tag{5}$$

where f^p represents the dilatational contribution to the field quantity, and f^s corresponds to the shear field contribution. The general 2D spectral representation of $f^j(\xi_1, \xi_2)$ is given by the inverse Fourier transform

$$f^j(\xi_1, \xi_2) = \frac{1}{2\pi} \int_{-\infty}^{\infty} \int_{-\infty}^{\infty} \hat{f}^j(k_x, k_y) \times e^{i[k_x \xi_1 + k_y \xi_2]} dk_x dk_y \tag{6}$$

where $j = p$ or $j = s$, and the frequency variables k_x and k_y are the Cartesian components of the plane wave propagation vector

$$\vec{k} = k_x \vec{e}_1 + k_y \vec{e}_2 \tag{7}$$

corresponding to each of the field quantities f^s or f^p, respectively. The angular frequency ω_j and the wave number $k = |\vec{k}|$ are related through the dispersion relation

$$\omega = C_j k \tag{8}$$

where we omit the use of subscripts for ω and k, and C_j represents the wave speed C_p or C_s, corresponding to the field component of interest. Next, consider that the propagating rupture is a source of waves moving along the x-axis at speed V_r, in which case the fault parallel phase velocity equals the steady state rupture speed, hence

$$\omega = k_x V_r \tag{9}$$

where $k_x = 2\pi/\lambda$. Combining Eq. (9) with the general dispersion relation Eq. (8) establishes a unique relationship between k_x and k_y given by

$$k_y = i\alpha_j k_x \tag{10}$$

where

$$\alpha_j = \sqrt{1 - \frac{V_r^2}{C_j^2}} \tag{11}$$

Note that α_j remains a real quantity if $V_r \leq C_j$. In particular, α_s remains real when rupture speeds are sub-shear, while α_p remains real when the rupture speed is sub-sonic. Moreover, since k_y is now expressed in terms of k_x, the general 2D spectral representation of $f^j(\xi_1, \xi_2)$ given by Eq. (6) simplifies to

$$f^j(x, y) = \frac{1}{\sqrt{2\pi}} \int_{-\infty}^{\infty} e^{-\alpha_j |k_x y|} \hat{f}^j(k_x) e^{ik_x(x)} dk_x \tag{12}$$

where $t = 0$ is now taken for the sake of convenience such that $\xi_1 = x - V_r t = x$, and $\xi_2 = |y|$ assures an exponential decay of the spectral field components with increased FN distance. The form of Eq. (12) corresponds to the representation of an evanescent wave in the Fourier domain. Rigorous derivations of evanescent wave fields arising from sub-Rayleigh ruptures have been previously established for a dislocation source model (Aki and Richards, 2002) as well as for dynamic rupture models (Kostrov, 1966; Kostrov et al., 1969; Kostrov and Nikitin, 1970; Freund, 1990; Broberg, 1999). Next, note that the source spectrum representation of the field component $f^j(x, y)$ is obtained by setting $y = 0$ in Eq. (12), in which case

$$f^j(x, 0) = \frac{1}{\sqrt{2\pi}} \int_{-\infty}^{\infty} \hat{f}^j(k_x) e^{ik_x(x)} dk_x \tag{13}$$

It then follows from the convolution theorem that

$$f^j(x, y) = \frac{1}{\sqrt{2\pi}} \int_{-\infty}^{\infty} f^j(x - \xi, 0) h(\xi, y) d\xi \tag{14}$$

where ξ is the integration variable and

$$h(\xi, y) = \frac{1}{\sqrt{2\pi}} \int_{-\infty}^{\infty} e^{-\alpha_j |k_x y|} e^{ik_x \xi} dk_x \tag{15}$$

represents the effective "impulse response" of the surrounding 2D linear elastic medium. An explicit form of the impulse response function, obtained by evaluating the Fourier transform expression (Eq. (15)), is given by

$$h(\xi, y) = \sqrt{\frac{2}{\pi}} \left[\frac{\alpha_j y}{(\alpha_j y)^2 + \xi^2} \right] \tag{16}$$

The magnitude and subsequent decay of the radiated P and S wave field contributions of a given stress or particle velocity field component with increased FN distance y from a steady state sub-Rayleigh rupture is thus governed by the convolution of the corresponding on-fault (source) field strength with the 2D impulse response function $h(\xi,y)$.

The radiated P-wave and S-wave fields arising from a rupture source are generally superimposed and not easily decomposed. The relative contribution of each radiation term at a given off-fault location is therefore difficult to assess unless a unique condition arises whereby one of the contribution field terms is absent. Such is the case, for example, at a field point taken sufficiently far from the fault where the dilatational field contribution has essentially vanished in comparison to the shear field radiation term. Another unique case applies to the dilatational field radiated by a supershear rupture ($C_s \leq V_r \leq C_p$), in which case the field strength outside of the shear Mach cone is described by the sub-sonic ($j = p$) form of the convolution integral (Eq. (14)). This point is re-addressed later in relation to experimental measurement of supershear ground motion signatures. Note that the evanescent wave field description, as expressed by (Eq. (14)), is strictly applicable to ruptures propagating under steady-state conditions. In fact, Madariaga (1977) shows that a decelerating or an accelerating rupture can emit high-frequency radiation into the medium and may no longer be subject to the above attenuation relationship. Bearing this point and other possible steady state rupture scenarios in mind, (Eq. (14)) nonetheless effectively demonstrates how a stress or particle velocity field component arising from a sub-Rayleigh rupture is destined to attenuate with increased FN distance. The result further demonstrates how high frequency content from a sub-Rayleigh rupture pulse source spectrum is rapidly stripped away with increased FN distance, thus making it very difficult to obtain detailed information about the breakdown zone from off-fault ground motion records (Dunham and Archuleta, 2005).

2.2. Fourier analysis of supershear rupture fields

In the case of a supershear rupture $C_s \leq V_r \leq C_p$, a unique condition arises whereby α_s becomes imaginary while α_p remains real. It is then convenient to define the quantity

$$\beta_s = \sqrt{\frac{V_r^2}{C_s^2} - 1} \qquad (17)$$

in place of α_s, which remains real for $C_s \leq V_r \leq C_p$, in which case

$$k_y^s = \beta_s k_x^s \qquad (18)$$

where the superscript s is now included in order to reinforce the fact that Eq. (18) applies strictly to the S-field contribution $f^s(x,t)$ while the dilatational field contribution f^p is still subject to decay as previously described. Substituting Eq. (18) for k_y in Eq. (6) leads to a spectral representation of the shear field contribution given by

$$f^s(\xi_1,\xi_2) = \frac{1}{\sqrt{2\pi}} \int_{-\infty}^{\infty} \hat{f}^s(k_x) e^{ik_x \xi_1} e^{ik_x \beta_s \xi_2} dk_x \qquad (19)$$

Note the absence of an attenuating factor in the Fourier transform relation, which clearly distinguishes this result from the sub-Rayleigh result Eq. (12). Application of the Fourier transform shift theorem now yields

$$f^s(\xi_1,\xi_2) = f^s(\xi_1 + \beta_s \xi_2) \qquad (20)$$

implying that the S-wave field remains unattenuated and radiates out to infinity along characteristic lines stemming from the rupture front defined by

$$\xi_1 + \beta_s \xi_2 = C \qquad (21)$$

Note that $C = 0$ since the origin of the coordinate system (ξ_1,ξ_2) is situated at the rupture tip. The equation of a characteristic line, which emanates from the rupture tip is thus given by

$$\xi_2 = -\frac{1}{\beta_s} \xi_1 \qquad (22)$$

from which it follows that

$$\tan\theta = \frac{1}{\beta_s} \qquad (23)$$

where θ is the acute angle between the x-axis and the S-wave characteristic as depicted in Fig. 3. Finally, from the definition of β_s, as expressed through Eq. (17), it is straightforward to show that

$$\tan\theta = \frac{C_s / V_r}{\sqrt{1 - C_s^2 / V_r^2}} \qquad (24)$$

which corresponds with the Mach cone half-angle relation Eq. (1). The S-wave field characteristics extending from the front and rear of the slip zone out to infinity are evidently Mach fronts, which bound the radiated S-wave field, as depicted in Fig. 3. The figure assumes $t = 0$ for the sake of convenience such that $\xi_1 = x - V_r t = x$, and $\xi_2 = y$. Note that the particle velocity and stress field components lying outside of the shear Mach cone must be purely dilatational in character and are therefore subject to attenuate in accordance with Eqs. (14) and (16), since α_p remains a real quantity. This point is emphasized by the point labeled (x_2,y_2) in Fig. 3. The results further imply that the near field region bounded by the leading and trailing slip zone Mach fronts comprises the unattenuated S-wave field and a superimposed, attenuating dilatational field as depicted at (x_1,y_1) in Fig. 3. Finally, at field points located far from the source where the dilatational field has decayed away, such as the point labeled (x_3,y_3) in Fig. 3, the field quantity $f(x_3,y_3)$ is shear field dominated and is essentially a scaled replica of the on-fault slip distribution (Dunham and Archuleta, 2005).

The notion of perfectly planar Mach fronts arising from a steady-state 2D rupture is a useful idealization. In actuality, a propagating supershear rupture may very well exhibit an unsteady rupture velocity history, characterized by an accelerating or decelerating rupture front, thereby leading to a curved Mach front profile as depicted in Fig. 4. In such cases the angle θ formed by a line drawn tangent to the Mach front at (x_1,x_2,t) is directly related to the rupture velocity at an earlier point in time $(x_1',0,t')$ in accordance with

$$f(x_1,y_1) = f^s(x,0) + \left[f^p(x,0) * h(x,y_1) \right]\big|_{x=x_1}$$

$$f^p(x_2,y_2) = f^p(x,0) * h(x,y_2)\big|_{x=x_2}$$

$$f(x_3,y_3) \approx f^s(x,0)$$

$$\vec{k}_s$$

$$x + \beta_s y = C$$

$$x + \beta_s y = C$$
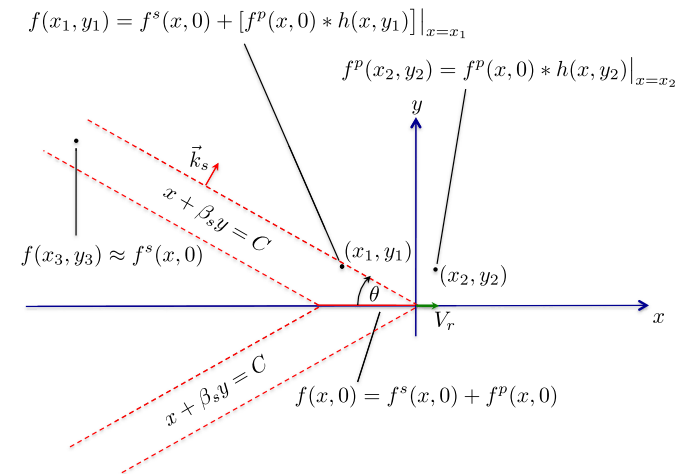
$$f(x,0) = f^s(x,0) + f^p(x,0)$$

Fig. 3. S-wave radiation from a supershear slip pulse propagated out to infinity along characteristics (Mach fronts).

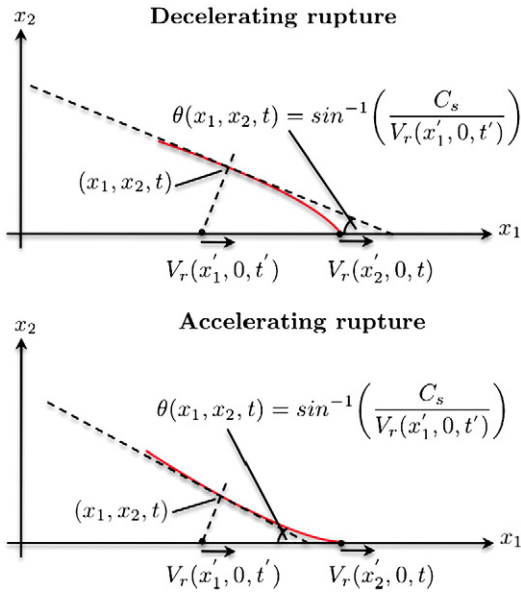Fig. 4. Curved Mach front profiles resulting from decelerating or accelerating supershear ruptures.

Fig. 5. Mach fronts arising from a supershear source propagated out to infinity along characteristics.

Eq. (25). In geometric terms, $(x_1', 0, t')$ is the point of intersection along the fault with a normal line drawn from the point of tangency (x_1, x_2, t) along the Mach front as depicted in the figures.

$$\theta(x_1, x_2, t) = \sin^{-1}\left[\frac{C_s}{V_r(x_1', 0, t')}\right] \tag{25}$$

2.3. Analysis of shear Mach fronts in the plane wave basis

Recall once again the inverse Fourier transform representation of an S-wave field quantity $f^s(\xi_1, \xi_2)$ given by

$$f^s(\xi_1, \xi_2) = \int_{-\infty}^{\infty} \hat{f}^s(k_x) e^{i[k_x \xi_1 + \beta_s k_x \xi_2]} dk_x, \tag{26}$$

arising from a 2D steady-state supershear rupture where $k_y = \beta_s k_x$. The supershear source spectrum representation, expressed by Eq. (26) represents the integration of all plane wave components having wave number $k = 2\pi/\lambda$, which collectively comprise $f^s(\xi_1, \xi_2)$ along the resulting shear Mach front. The contribution from an individual plane wave component, having wave number $k = 2\pi/\lambda$, is therefore given by

$$df^s(\xi_1, \xi_2) = \hat{f}^s(k_x) e^{i[k_x \xi_1 + \beta_s k_x \xi_2]} dk_x \tag{27}$$

This representation effectively defines the plane wave basis, which provides a convenient means of analyzing the displacement or stress field components along a shear Mach front. Fig. 5 depicts a pair of planar shear Mach fronts stemming from a supershear slip pulse propagating in the positive x-direction. A single plane wave contribution (of wavelength λ), to the shear displacement field along the Mach front may then be expressed as

$$u^s(\xi_1, \xi_2; \lambda) = \hat{u}^s(\lambda) e^{i[k_x \xi_1 + \beta_s k_x \xi_2]} \tag{28}$$

where the differential notation has been dropped for the sake of convenience and the symbol $\hat{u}^s(\lambda) = \hat{u}^s(k_x) dk_x$ has been adopted to denote the fact that we are actually referring to a single wavelength contribution of the entire plane wave spectrum. All of the wavelength
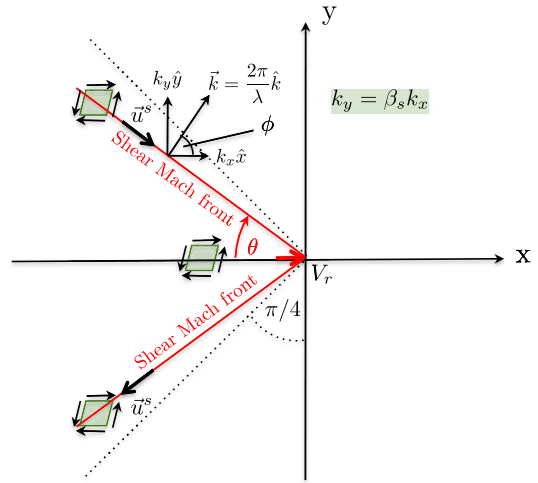
contributions to the displacement field $u^s(\xi_1, \xi_2)$ along the shear Mach front are represented by similar plane wave expressions, which may differ in amplitude depending upon the functional nature of the rupture source spectrum. The individual plane wave components, each defined by a wave vector $\vec{k} = (2\pi/\lambda)\hat{k}$, are all superimposed in space with their unit vectors $\hat{k}$ oriented normal to the shear Mach front and inclined at an angle ϕ with respect to the x-axis as depicted in Fig. 5. Note that $t = 0$ is assumed for the sake of convenience such that $\xi_1 = x - V_r t = x$, and $\xi_2 = y$. Next, consider the plane wave basis representation of the FP and FN displacement components, u_x^s and u_y^s, which may be expressed as

$$u_x^s(\xi_1, \xi_2; \lambda) = \hat{u}_x^s(\lambda) e^{i[k_x \xi_1 + \beta_s k_x \xi_2]} dk_x \tag{29}$$

$$u_y^s(\xi_1, \xi_2; \lambda) = \hat{u}_y^s(\lambda) e^{i[k_x \xi_1 + \beta_s k_x \xi_2]} dk_x \tag{30}$$

Invoking Eq. (4) along with Eqs. (29) and (30) in the plane wave basis leads to

$$\nabla \cdot \vec{u}_\lambda^s = ik_x u_x^s(\lambda) + i\beta_s k_x u_y^s(\lambda) = 0 \tag{31}$$

Substituting Eq. (18) then leads to

$$u_x^s(\lambda) = -\beta_s u_y^s(\lambda) \tag{32}$$

The expression immediately reveals that $|u_y^s| > |u_x^s|$ (FN component dominates over FP component) when $0 \leq \beta_s < 1$, corresponding to the rupture speed regime ($C_s \leq V_r < \sqrt{2}C_s$), whereas $|u_x^s| > |u_y^s|$ (FP component dominates over FN component) when $1 < \beta_s \leq \sqrt{(C_p/C_s)^2 - 1}$, corresponding to the speed regime ($\sqrt{2}C_s < V_r \leq C_p$). Special cases of interest that limit the upper bound of β_s in the stable rupture speed regime are (1) if $C_p = \sqrt{3}C_s$, often assumed for crustal rock, whereby $1 < \beta_s \leq \sqrt{2}$, and (2) $C_p \approx 2C_s$, applicable to H-100 test specimens used in laboratory earthquake experiments, whereby $1 < \beta_s \leq \sqrt{3}$. The two Mach angle domains bounded to either side of $\theta = \pi/4$ are graphically depicted in Fig. 6. Once again, $t = 0$ is assumed for the sake of convenience such that $\xi_1 = x - V_r t = x$, and $\xi_2 = y$. The right hand diagram demonstrates how the fault parallel velocity component dominates over the FN velocity component along the shear Mach front in the stable supershear regime ($\theta < \pi/4$), whereas the opposite case applies in the left hand diagram, corresponding to the unstable rupture speed regime ($\theta > \pi/4$). Note as well how the direction of the displacement vector $\vec{u}_s$ is depicted pointing upward along the shear
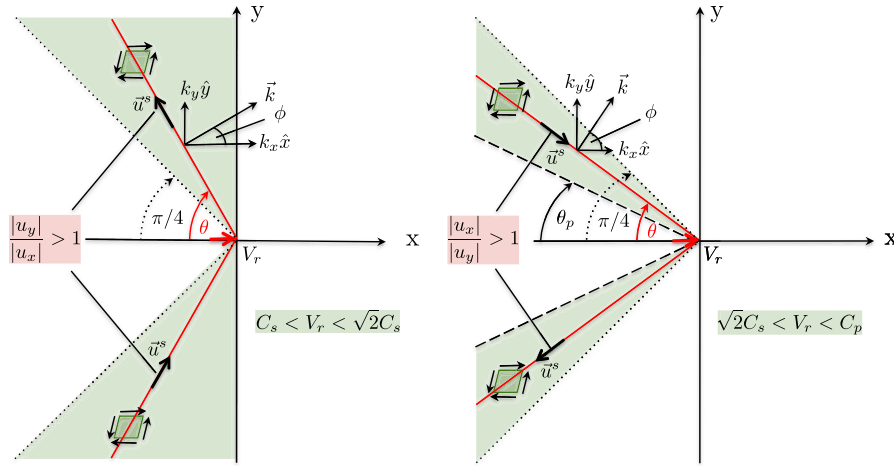
Fig. 6. Range of Mach angles corresponding to each of the supershear rupture speed regimes.

Mach front in the left hand diagram where $\theta > \pi/4$, as opposed to pointing downward along the Mach front as depicted in the right hand diagram where $\theta < \pi/4$, in accordance with the sense of motion of the contributing shear wavelets at points of tangency to the Mach front. Following the Poisson displacement field decomposition Eq. (2), the radiated strain field tensor arising from a supershear rupture may then also be expressed as the sum of shear and dilatational field contributions

$$\varepsilon_{ij} = \varepsilon_{ij}^s + \varepsilon_{ij}^p \qquad (33)$$

Application of the strain-displacement relations applied to the plane wave basis expressions (Eqs. (29) and (30)) and combining with Eq. (32) leads to the strain field components of the S-wave field term given by

$$\varepsilon_{11}^s(\lambda) = ik_x u_x^s(\lambda) \qquad (34)$$

$$\varepsilon_{22}^s(\lambda) = -ik_x u_x^s(\lambda) = -\varepsilon_{11}^s(\lambda) \qquad (35)$$

$$\varepsilon_{12}^s(\lambda) = \frac{i\mu k_x}{2} u_x^s(\lambda)\left[\beta_s - \frac{1}{\beta_s}\right] \qquad (36)$$

Application of Hooke's law and invoking the fact that $\varepsilon_{kk}^s = 0$ leads to S-wave field stress tensor

$$\sigma_{ij}^s(\lambda) = 2\mu\varepsilon_{ij}^s(\lambda) \qquad (37)$$

When $V_r = \sqrt{2}C_s$ corresponding to $\theta = \pi/4$, it follows from Eq. (32) that $u_x^s = -u_y^s$, since $\beta_s = 1$. Combining this with the fact that $\vec{u}^s$ reverses direction at $\theta = \pi/4$, in accordance with the double-couple solution (Aki and Richards, 2002) (graphically reinforced in Fig. 1), implies that $u_x^s = u_y^s = 0$ and thus $\vec{u}^s = 0$ at this unique rupture speed. Hence, by Eqs. (34), (35) and (36) it follows that σ_{ij}^s, will also vanish when $V_r = \sqrt{2}C_s$, thus leaving only a dilatational stress field contribution, which curls around the slip zone and eventually attenuates with off-fault distance. Simply stated, a supershear rupture will not radiate any S-waves into the surrounding medium when $V_r = \sqrt{2}C_s$. The result is consistent with the fact that the locus of points that collectively comprise the Mach front at this rupture speed are the nodal points corresponding to $\phi = \pi/4$ on the shear wavelets as depicted in Fig. 1. The vanishing of all S-wave radiation at $V = \sqrt{2}C_s$, as motivated here using a simple spectral analysis, also emerges from the full elastodynamic solution for a 2-D steady state rupture subject to a prescribed shear traction $\tau(x)$ along the frictional fault as addressed in the following section.

A continuum mechanics based treatment of the significance of the rupture speed $V_r = \sqrt{2}C_s$ in isotropic, steady-state elastodynamics problems is found in Liu et al. (1995) and Gao et al. (1999). In particular, the paper by Liu et al. (1995) uses continuum mechanics to show that a shear Mach front features jumps in shear stress and particle velocity. These jumps are shown to disappear when the rupture speed reaches $V_r = \sqrt{2}C_s$. Consistent with the above discussion, the work of Gao et al. (1999) uses a continuum mechanics approach to identify radiation-free stress states for various steady-state, linear elastodynamics problems including dislocations and cracks. Here again the unique rupture speed $V_r = \sqrt{2}C_s$ emerges as one which corresponds to "radiation free" growth of dynamically propagating singularities.

2.4. Ground motion signatures in the sub-Rayleigh rupture speed regime

2.4.1. Singular linear elastic solution for a shear crack in the sub-Rayleigh regime: $V_r < C_R$

Freund (1979, 1990) rigorously solved the 2D plane strain elastodynamic problem of a dynamically propagating shear (mode II) crack in a linear elastic half-space. The problem was posed in a Cartesian coordinate frame with the crack front oriented parallel to the x_3 axis such that the displacement field $\vec{u} = \vec{u}(x_1, x_2)$. The crack was assumed to propagate strictly along the x_1 direction with crack tip coordinates given by $(x_1 = l(t), 0)$ where $l(t)$ is a continuous function of time. The instantaneous crack tip speed is then given by $V_r(t) = \dot{l}(t)$. A local coordinate system (ξ_1, ξ_2) was then introduced with the origin selected to coincide with the crack tip such that $\xi_1 = x_1 - l(t)$ and $\xi_2 = x_2$. A local polar coordinate system (r, θ) was also introduced whereby $r = \sqrt{\xi_1^2 + \xi_2^2}$ and $\theta = \tan^{-1}(\xi_2/\xi_1)$. By imposing the steady-state assumption and taking the origin of anew coordinate system to coincide with the crack tip, the governing wave equation expressions for the dilatational displacement potential ϕ and shear displacement potential ψ become two-dimensional in $\xi = x - V_r t$ and $\xi_2 = y$ under a Galilean coordinate transformation. The derivation ultimately leads to a standard Hilbert problem in analytic function theory, which is solved subject to the prescribed traction free boundary conditions on the crack surfaces, in order to obtain the asymptotic stress and particle velocity field solutions. The singular elastic (asymptotic) solution for the particle velocity field components $\dot{u}_1(r, \theta)$ and $\dot{u}_2(r, \theta)$ are given by

$$\dot{u}_1 = -sgn(\xi_2)\frac{V_r \alpha_s K_{II}(t)}{\mu D\sqrt{2\pi r}}\left[2\frac{\sin\frac{1}{2}\theta_p}{\sqrt{\gamma_p}} - \left(1 + \alpha_s^2\right)\frac{\sin\frac{1}{2}\theta_s}{\sqrt{\gamma_s}}\right] \qquad (38)$$

and

$$\dot{u}_2 = -\frac{V_r K_{II}(t)}{\mu D \sqrt{2\pi r}} \left[2\alpha_p \alpha_s \frac{cos\frac{1}{2}\theta_p}{\sqrt{\gamma_p}} - \left(1 + \alpha_s^2\right) \frac{cos\frac{1}{2}\theta_s}{\sqrt{\gamma_s}} \right] \qquad (39)$$

where $K_{II}(t)$ is the instantaneous mode II stress intensity factor, μ is the shear modulus, and α_s, α_p are given by Eq. (11). $sgn(x)$ is the signum function, which is equal to $+1$ for $x>0$ and -1 for $x<0$. The remaining factors D, θ_p, θ_s, γ_d, and γ_s are given by

$$D = 4\alpha_p \alpha_s - \left(1 + \alpha_s^2\right)^2 \qquad (40)$$

where D is the Rayleigh function and $D \rightarrow 0$ as $V_r \rightarrow C_R$

$$\theta_p = tan^{-1}\left(\alpha_p tan\theta\right); \quad \theta_s = tan^{-1}(\alpha_s tan\theta) \qquad (41)$$

and finally,

$$\gamma_p = \sqrt{1 - \left(V_r sin\theta / C_p\right)^2}$$
$$\gamma_s = \sqrt{1 - (V_r sin\theta / C_s)^2} \qquad (42)$$

2.4.2. Dominance of the FN component in the sub-Rayleigh rupture speed regime

Fig. 7 displays the particle velocity field $\vec{u}(\xi_1, \xi_2)$ in the immediate neighborhood of a dynamic shear crack propagating at $V_r = 0.875C_s$. The colors correspond to $|\vec{u}|$ while the white arrows of constant magnitude form a streak plot, which indicates the sense of motion throughout the field. The plot corresponds to a right lateral shear rupture, as indicated by the sense of particle motion above and below the crack plane (dashed black line in the figure). The most obvious and striking feature of the result is dominance of the FN particle velocity component over the FP velocity component for $\xi_1>0$ as revealed by the inclination of the velocity vectors, which are predominantly pointing in the vertical direction. Particle velocity records acquired at the two fictitious measurement stations displayed
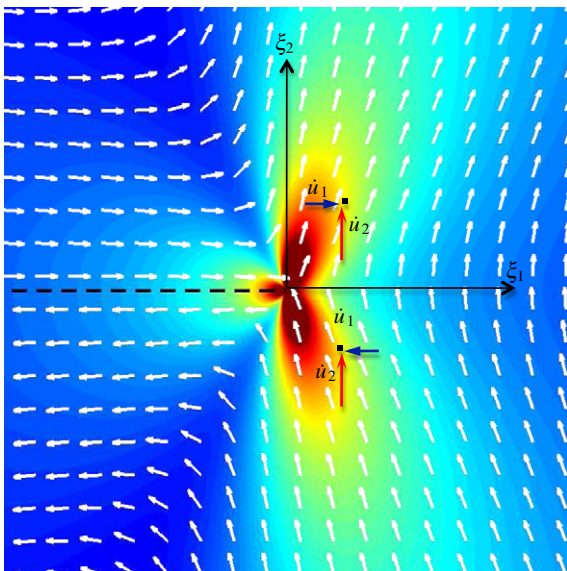

Fig. 7. The near tip particle velocity field for a shear crack propagating at $V_r = 0.875C_s$.

in the figure are thus expected to exhibit a FN velocity swing which dominates in magnitude over the FP velocity swing i.e.,

$$|\dot{u}_{2_{max}} - \dot{u}_{2_{min}}| > |\dot{u}_{1_{max}} - \dot{u}_{1_{min}}|, (V_r < C_R) \qquad (43)$$

as the sub-Rayleigh crack tip field sweeps through each respective station. Apart from the fact that the solution exhibits a sharp singularity at $r=0$ and that it lacks a meaningful length scale, the general signature of the resulting particle velocity field in the neighborhood of advancing crack tip is nonetheless representative of the particle velocity resulting from a sub-Rayleigh rupture. Similar ground motion signatures associated with sub-Rayleigh rupture propagation in natural earthquakes, which feature a dominant FN motion component, were numerically demonstrated by Aagaard and Heaton (2004) using a kinematic rupture model. Rigorous elastodynamic solutions, which consider the frictional fault resistance between the shear crack faces and a cohesive (breakdown) zone ahead at the rupture front, also lead to particle velocity field solutions featuring a dominant FN component, particularly in the half-space $\xi_1>0$ situated ahead of the advancing rupture front (Dunham and Archuleta, 2005). A major distinction of these solutions over the singular elastic solution for a propagating shear crack, is the emergence of a meaningful length scale, resulting from an assumed length of the break down zone.

2.4.3. Singular linear elastic solution for a shear crack in the supershear regime: $C_s \leq V_r \leq C_p$

Freund (1979, 1990) also considered the elastodynamic solution for a dynamic shear crack propagating into the supershear rupture speed regime subject to the same coordinate frame description and traction free boundary conditions as were assumed in the sub-Rayleigh problem. The closed form solution that emerges for the particle velocity components $\dot{u}_1$ and $\dot{u}_2$ is conveniently expressed as the sum of a dilatational and shear field contribution

$$\dot{u}_j = AV_r\left(\dot{u}_j^p + \dot{u}_j^s\right) \qquad (44)$$

where $j=1,2$ and A represents a stress intensity factor. The dilatational field contributions to the FP and FN particle velocity components are given by

$$\dot{u}_1^p = \frac{sin\left(q\theta_p\right)}{r_p^q} \quad ; \quad \dot{u}_2^p = -\alpha_p \frac{cos\left(q\theta_p\right)}{r_p^q} \qquad (45)$$

with variables r_p and q given by

$$r_p = \sqrt{\xi_1^2 + \left(\alpha_p \xi_2\right)^2} \qquad (46)$$

$$q = \frac{1}{\pi} tan^{-1}\left[\frac{4\alpha_p \beta_s}{(2 - V_r^2/C_s^2)^2}\right] \qquad (47)$$

Note that $0 \leq q \leq 1/2$ and that the value $q=1/2$ is only attained when $V_r = \sqrt{2}C_s$ where the S-wave field is known to vanish. Hence, the singularity introduced by the exponent q is notably weaker than the $r^{-1/2}$ singularity, which arises in the sub-Rayleigh solution.

The shear field contributions to the FP and FN particle velocity components are given by

$$\dot{u}_1^s = -sgn(\xi_2)\frac{\beta_s^2\left(2 - \frac{V_r^2}{C_s^2}\right)sin(\pi q)}{2\beta_s(|\xi_1 + \beta_s\xi_2|)^q} \times H(-\xi_1 - \beta_s|\xi_2|) \qquad (48)$$

and

$$\dot{u}_2^s = \frac{\left(2-\frac{V_r^2}{C_s^2}\right)sin(\pi q)}{2\beta_s(|\xi_1 + \beta_s\xi_2|)^q}H(-\xi_1-\beta_s|\xi_2|) \qquad (49)$$

where $sgn(x)$ is the signum function, which is equal to $+1$ for $x>0$ and -1 for $x<0$.

2.4.4. Particle motion along a Mach front in the supershear regime: $C_s \leq V_r \leq C_p$

The particle velocity field plots depicted in Fig. 8 correspond to four different crack tip speeds, which collectively span the entire supershear rupture speed regime. Each plot corresponds to a right lateral rupture of a shear crack, which is represented by the dashed black line. The colors correspond to $|\dot{\vec{u}}|$ while the white arrows of constant magnitude form a streak plot, which only reveal the sense of motion throughout the field. The plot in Fig. 8(a), corresponding to $V_r = 1.005C_s$, highlights how the shear Mach angle approaches $\theta = \pi/2$ in the limit that $V_r \rightarrow C_s$. Note the dominance of the FN particle velocity component over the FP component along the shear Mach front, as expected in the unstable portion of the supershear rupture speed

regime $\left(C_s \leq V_r < \sqrt{2}C_s\right)$. Care should be taken not to confuse the sense of motion suggested by the vectors on the purely dilatational side of the velocity field as indicative of motion along the shear Mach front. The direction and sense of rotation of the vector field in the wake of the rupture, where the field is shear dominated, reveals how particle motion is directed upwards along the shear Mach front. The particle velocity field is evidently characterized by a sharp reversal in the particle velocity field across the Mach front between the shear dominated side and the purely dilatational region ahead of the Mach front.

Fig. 8(b) corresponds to a supershear rupture speed $V_r = 1.25C_s$. Note how the Mach angle has decreased with increased rupture speed but is still inclined such that $\theta > \pi/4$ and that the particle velocity field along the shear Mach front is still dominated by the FN component. Particle motion along the shear Mach front is still directed upwards along the shear Mach front, as revealed by the direction and sense of rotation of the velocity vector field in the wake of the rupture tip.

The shear Mach fronts in frames (a) and (b) are both shown crossing hypothetical particle velocity measurement stations situated above and below the crack plane with red and blue arrows representing the FN and FP velocity components, respectively. Particle velocity records acquired at these locations are thus expected to
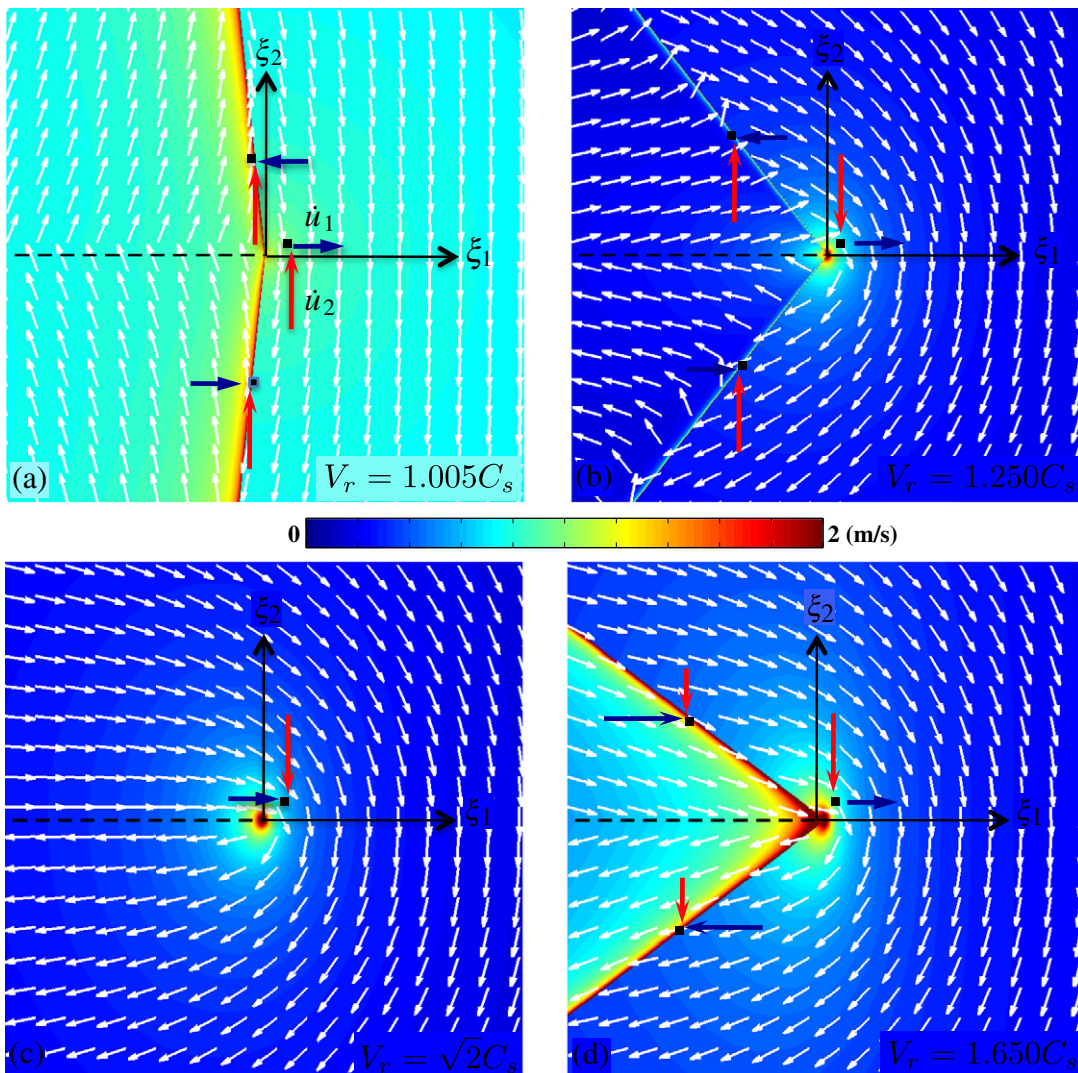

Fig. 8. Singular elastic particle velocity field plots for a supershear crack propagating at (a) $V_r = 1.005C_s$, (b) $V_r = 1.250C_s$, (c) $V_r = \sqrt{2}C_s$, (d) $V_r = 1.650C_s$. The vectors depict only the direction of the velocity field.

exhibit a sharp positive FN velocity swing which dominates in magnitude over the FP velocity swing i.e.,

$$|\dot{u}_{2_{max}} - \dot{u}_{2_{min}}| > |\dot{u}_{1_{max}} - \dot{u}_{1_{min}}|, \left(C_s \leq V_r < \sqrt{2}C_s\right) \tag{50}$$

Finally, note the presence of the purely dilatational field, which circulates about the crack tip and extends out a short distance out beyond the Mach front before rapidly attenuating. A hypothetical near field measurement station, lying close to the crack plane and situated ahead of the advancing Mach front, should thus record an initial velocity swing induced by the passage of the locally concentrated dilatational field, followed by a sharp, positive velocity jump in the FN component as the shear Mach front crosses the station.

Fig. 8(c) corresponds to the unique case corresponding to $V_r = \sqrt{2}C_s$ whereby the shear Mach front has now completely vanished as expected and previously predicted using a simple 2D steady-state spectral analysis. At this unique rupture speed, energy that would be otherwise radiated into the medium in the form of shear waves is instead converted into fracture energy. Note that the only radiation term arising from the crack tip is in the form of dilatational waves, as revealed by the concentrated field surrounding the crack tip, which rapidly attenuates with off-fault distance.

Finally, consider Fig. 8(d) corresponding to a supershear rupture speed $V_r = 1.65C_s$ whereby the rupture speed has now crossed over the $V_r = \sqrt{2}C_s$ threshold. Note the dominance of the FP particle velocity component over the FN component along the shear Mach front for $\theta < \pi/4$, as expected in the rupture speed regime $\left(\sqrt{2}C_s < V_r \leq C_p\right)$. Particle motion along the shear Mach front is now directed downward along the shear Mach front, as revealed by the direction and sense of rotation of the velocity vector field in the wake of the rupture where the field is shear dominated. It is interesting to note how the particle velocity field vectors on either side of the Mach front are now aligned in the same direction indicating that there is no longer a sharp reversal in the particle velocity field across the Mach front, which occurs in the unstable rupture speed regime $C_s \leq V_r < \sqrt{2}C_s$. As with frames (a) and (b), the shear Mach fronts are shown crossing fictitious particle velocity measurement stations situated above and below the crack plane with red and blue arrows representing the FN and FP velocity components, respectively. Particle velocity records acquired at these locations are thus expected to exhibit a sharp positive FP velocity swing which dominates in magnitude over the FN velocity swing i.e.,

$$|\dot{u}_{1_{max}} - \dot{u}_{1_{min}}| > |\dot{u}_{2_{max}} - \dot{u}_{2_{min}}|, \left(\sqrt{2}C_s < V_r \leq C_p\right) \tag{51}$$

Note the concentrated dilatational field, which is spread out over a larger spatial extent and visibly contracted along the propagation direction at this increased rupture speed. A hypothetical near field measurement station lying close to the crack plane and situated ahead of the advancing Mach front should again record a dilatational precursor signal, followed by a sharp, positive velocity jump in the FP component as the shear Mach front crosses the station.

2.5. Steady-state cohesive zone models

The main underlying assumption in the singular elastic crack models discussed earlier is that the inelastic breakdown processes associated with the crack tip are confined to its vicinity. Such models do not allow, nor do they take into account the change in the tractions which occur in such breakdown zones. By adopting an approach that was analogous to the cohesive zone models for tensile cracks developed by Dugdale (1960) and Barenblatt (1962), Ida (1972) and Palmer and Rice (1973) introduced the non-singular slip-weakening model for shear, or Mode II, cracks that provides a description of the tractions in the cohesive zone.

In these models the shear traction along the crack undergoes a weakening or degradation process which begins when the shear stress reaches a finite material peak strength ahead of the crack tip and continues to degrade with increasing amount of slip, approaching a residual level of shear strength. This results in a spatial degradation of the shear strength behind the crack-tip. This also introduces a characteristic length scale into the analysis, which is missing in the singular elastic models. The resulting length scale is proportional to the size of the breakdown/process zone behind the crack tip and varies with the speed of the crack tip. Samudrala et al. (2002a,b) applied a slip velocity dependent shear strength breakdown law, commonly referred to as the velocity-weakening friction law, and obtained steady-state solutions to the propagating sub-Rayleigh and supershear Mode II crack problems. All of the above problems feature steady-state solutions that depend on the real and imaginary parts of the following integral (see Muskhelishvili, 1953; Broberg, 1978, 1989, 1999).

$$M\left(z_{p/s}\right) = c_1 \left[\Omega\left(z_{p/s}\right)\right]^q \int_\Gamma \frac{\tau(w)}{\left[\Omega_+(w)\right]^q \left(w - z_{p/s}\right)} dw \tag{52}$$

where Ω is an analytic function with branch cuts along the crack (or pulse), Γ, c_1 depends on the rupture speed and q is the rupture speed dependent exponent (Eq. (47)). $\tau(x)$ is either prescribed a-priori in slip-weakening like models or for slip-velocity weakening models is obtained by solving a singular integral equation (Samudrala et al., 2002a,b). This integral is evaluated in the Cauchy Principal Value sense and has analytical closed form solutions for certain forms of $\tau(x)$ and sub-Rayleigh rupture velocities. For supershear cases the closed form solution exists only for constant $\tau(x)$, i.e. $\tau(x) = \tau_p$. Dunham and Archuleta (2005), extended the steady-state sub-Rayleigh slip pulse model of Rice et al. (2005) to the supershear rupture velocity domain. A solution was obtained for a rupture/slip pulse of finite length L propagating at a steady-state rupture velocity V_r along a frictional fault plane with a prescribed shear traction $\tau(x)$ that degraded linearly with distance, up to a residual level, behind the rupture tip. Results of the derivation identified, for the first time, a remarkable feature that the shear contribution to the particle velocity field scales directly with the slip-velocity variation along the pulse as expressed by Eqs. (53) and (54).

$$\dot{u}_x = -\frac{V_r}{\mu}\left[\frac{1}{2\alpha_d}\Im M\left(z_p\right)\right] + \frac{\beta_s^2 - 1}{2(\beta_s^2 + 1)}\Delta\dot{u}_x(z_s) \tag{53}$$

$$\dot{u}_y = -\frac{V_r}{\mu}\left[\frac{1}{2}\Re M\left(z_p\right)\right] - \frac{1}{2\beta_s}\frac{\beta_s^2 - 1}{\beta_s^2 + 1}\Delta\dot{u}_x(z_s) \tag{54}$$

where $\Delta\dot{u}_x = \dot{u}_x(x, 0^+) - \dot{u}_x(x, 0^-)$ is the slip velocity variation along the pulse and $z_s = x + \beta_s|y|$. Due to the finite crack-tip stresses and a finite width process zone, the passage of the Mach front results in particle velocity jumps that are of finite width and magnitude, unlike the singular elastic crack models. Also, in stark contrast to the singular models, the crack-tip energy flux is non-zero and finite in the supershear regime (Broberg, 1989; Samudrala et al., 2002a,b; Rosakis et al., 2007).

Far from the fault, where the dilatational contribution has decayed away, the fault parallel and fault normal particle velocity components along the shear Mach front reduce to

$$\dot{u}_x \approx \frac{1}{2}sgn(y)\frac{\beta_s^2 - 1}{\beta_s^2 + 1}\Delta\dot{u}_x(z_s) \tag{55}$$

$$\dot{u}_y \approx -\frac{1}{2\beta_s}\frac{\beta_s^2 - 1}{\beta_s^2 + 1}\Delta\dot{u}_x(z_s) \tag{56}$$

The $sgn(y)$ function is simply introduced in order to account for regions above or below the fault. Note in particular how $\dot{u}_x = -\beta_s \dot{u}_y$ is precisely recovered, far from the fault, as was previously shown by the simple 2D steady-state spectral analysis and furthermore how the presence of β_s and the sign of the slip velocity function $\Delta \dot{u}_x$ in Eqs. (55) and (56) completely determine the sign and magnitude of the fault parallel and fault normal ground motion components along the shear Machfront. Perhaps most significantly, the results demonstrate that the far field ground motion components resulting from the passage of a shear Mach front correspond to a scaled replica of the slip velocity function back along the slip zone. We note that this is a general feature of all steady-state Mode II cohesive zone solutions (Broberg, 1989; Samudrala et al., 2002a; Dunham and Archuleta, 2005) irrespective of the details of the cohesive zone law used. This characteristic of supershear S-wave radiation is in stark contrast to the nature of S-wave radiation arising from sub-Rayleigh ruptures, which is stripped of high frequency content and attenuates rapidly with off-fault distance.

The analysis considered thus far is a 2D approximation to a 3D problem. In reality, 3D effects along with other attenuating factors will ultimately conspire to attenuate the shear Mach front in the far field. Bhat et al. (2007) estimated that a reasonable attenuation distance should be of the order of the depth of the seismogenic zone. Dunham and Bhat (2008) conducted a numerical 3D steady-state analysis of supershear ruptures and showed that this is indeed the case. Nonetheless, it stands to reason that supershear ruptures should have a more far reaching influence into the surrounding medium and an increased propensity to perturb the stress state of neighboring faults, compared to subshear ruptures of equivalent magnitude. This point has been partly observed by Bouchon and Karabulut (2008) who showed that the aftershocks cluster in a region away from the fault at distances comparable to the depth of the seismogenic zone following the passage of a supershear rupture.

The various rupture models discussed above show that in the rupture speed regime $\sqrt{2}C_s < V_r \leq C_p$, the ground motion carried by the shear Mach front is characterized by a fault parallel (FP) particle velocity swing which dominates in magnitude over the fault normal (FN) velocity swing. The opposite case is shown to hold true in the rupture speed regime $C_s \leq V_r < \sqrt{2}C_s$ where the FN velocity swing dominates in magnitude over the FP velocity swing. In both cases, the FN and FP ground motion components are predicted to be opposite in sign. A similar analysis applied to sub-Rayleigh ruptures predicts ground motion records, in regions ahead of the rupture front, that are characterized by a FN velocity swing which dominates in magnitude over the FP velocity swing.

Since S-wave radiation from a supershear rupture is confined to the region behind the leading shear Mach front, the region lying outside these Mach fronts experiences only the dilatational field associated with the crack-tip. This is a unique signature of the supershear regime. Near-source ground motion records corresponding to the passage of the shear Mach front are however, influenced by the presence of the superimposed dilatational field, which circulates all the way around the slip zone. Synthetic ground motion records derived from these models predict a short pronounced peak, particularly in the FP record, signaling the passage of the leading dilatational field prior to the arrival of the shear Mach front. A similar effect, although less pronounced, is observed in the corresponding FN ground motion records. At greater and greater off-fault distances, there will also be an increased separation in time between the arrival of the leading dilatational field and the arrival of the fault parallel velocity jump associated with the arrival of the shear Mach front. As discussed earlier, the leading dilatational field will tend to rapidly attenuate with increased off-fault distanced in accordance with Eq. (16) leaving only an S-wave field contribution to the Mach front in the far field, which theoretically carries information directly related to the slip velocity variation back at the fault.

2.6. Unsteady cohesive zone models and trailing Rayleigh rupture

Close scrutiny of the entire class of self-similar analytical solutions for supershear ruptures (for e.g. Burridge, 1973; Broberg, 1994) also reveals that a secondary peak in the slip velocity travels behind the main crack-tip at the Rayleigh wave speed. This feature, herein referred to as a trailing Rayleigh disturbance, also accompanies spontaneously propagating ruptures and cannot be captured by steady-state models. The trailing Rayleigh disturbance represents the region behind the crack-tip where Rayleigh waves, emitted from the process zone of the crack tip, coalesce and depending on the friction conditions result in a secondary rupture. Its strength is also expected to depend on the speed of the main crack-tip, nature of the main rupture (pulse-like or crack-like), size of the process zone and the strength/stress drop associated with it.

Figs. 9 and 10 are useful for graphically illustrating the general sense of particle motion for spontaneous right lateral sub-Rayleigh and supershear ruptures subject to a slip-weakening friction law. These results were numerically simulated using a commercial Finite Element code, ABAQUS. Bilateral ruptures are depicted in the figure as generally encountered in laboratory earthquake experiments. The sense of particle motion is reasoned as follows. In the case of sub-Rayleigh ruptures (Fig. 9), the FN component is dominant near the rupture tip, as expected from earlier, more elementary discussions. Since no opening is allowed, the FN component does not change sign as one crosses the fault. The direction of the velocity vector near the rupture tip depends, obviously, on whether the domain is under compression or extension in the FN direction. Also, since this is a crack-like rupture, there is continuous sliding behind the rupture-tip. For supershear ruptures (Fig. 10) the dominant sense of motion near the crack-tip is FP, as expected in the stable rupture velocity regime. The sense of motion of the FP component mimics the right-lateral nature of the rupture as expected. One also notices that the leading dilatational field (just outside the Mach front) exhibits a dominant FP component in the near field. The supershear rupture-tip is then followed by the trailing Rayleigh disturbance which results in a dominant FN sense of motion. The sense of motion of this pulse is exactly the same as that for a sub-Rayleigh rupture. Depending on the governing friction law, both the main rupture and the trailing Rayleigh disturbance could be pulses in the strictest sense of the word i.e. the fault is locked from slipping in their wake or they could be both crack-like ruptures or a combination of crack-like and pulse-like rupture. Regardless of whether it is a pulse, crack, or wave like disturbance, both theory and experiment show that under certain conditions, supershear ruptures may be quickly followed by a trailing disturbance, propagating at the Rayleigh wave speed, which can induce the ground motion signature of a strong sub-Rayleigh rupture. This scenario and its associated ground motion signatures are extremely relevant and important to study from a seismic hazard perspective.

In principal, each of the aforementioned field disturbances and ground motion signatures arising from the passage of a supershear rupture can be uniquely identified in ground motion records. In later sections we demonstrate how these features can be reproduced and documented in laboratory earthquake experiments using high speed photoelastic imaging techniques for full field visualization and high bandwidth heterodyne interferometer systems for continuous particle velocity records at fixed positions adjacent to a frictional fault on the surface of a model test specimen.

3. Laboratory earthquake experiment

Nearly two and one-half decades following theoretical and numerical predictions by Burridge (1973) and Andrews (1976), experimental verification of supershear ruptures was first achieved by Rosakis and coworkers both in relation to bimaterial systems
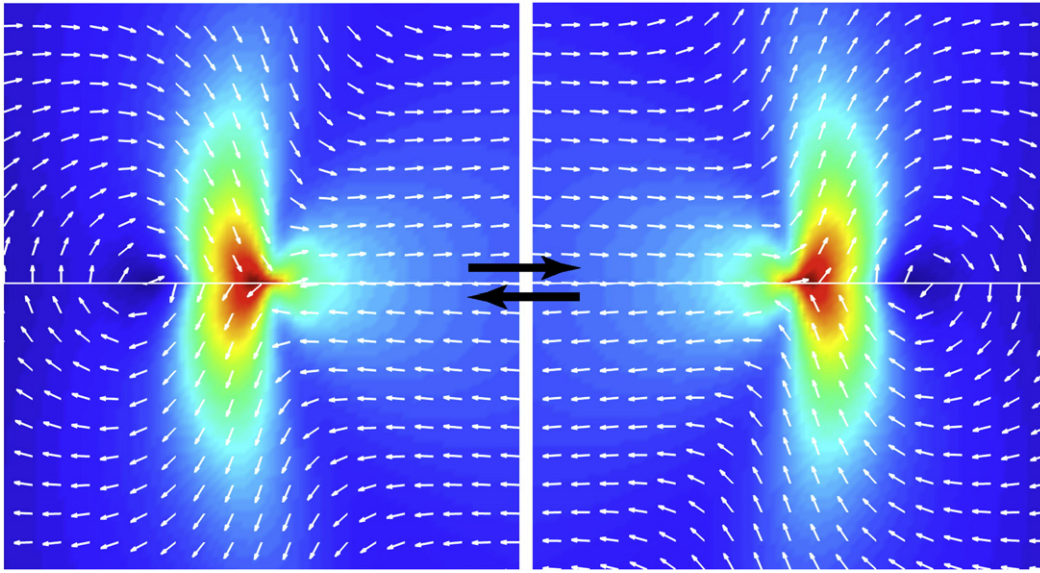
Fig. 9. Sense of particle motion for a spontaneous right-lateral sub-Rayleigh rupture. The contour plot shows the magnitude of the velocity field and the vectors show only the sense of motion.

(Lambros and Rosakis, 1995; Liu et al., 1995; Rosakis et al., 1998; Coker et al., 2005; Xia et al., 2005b; Lykotrafitis and Rosakis, 2006; Lykotrafitis et al., 2006a,b) and also in relation to homogeneous systems containing weak planes (Rosakis et al., 1999, 2007). Later work by Rosakis and co-workers focused exclusively on the study of purely frictional ruptures utilizing a novel laboratory earthquake experiment, which featured a dynamic rupture along an inclined, frictional interface formed by two compressed quadrilateral sections of Homalite™ (H-100), an optically transparent, stress-birefringent, and mildly rate sensitive brittle polyester resin.

A schematic depiction of the H-100 specimen geometry, static loading configuration, and dynamic rupture nucleation scheme is shown in Fig. 11. The mating edges of two quadrilateral test sections are initially polished to a near optical grade finish in order to remove surface defects from the CNC milling operation. The surfaces are then roughened using a micro-bead blasting treatment using an abrasive media comprised of tiny glass beads with diameters ranging from $43 \mu m - 89 \mu m$ (170–325 mesh size). Precise repetition of the bead blasting procedure from specimen to specimen assures a consistent surface roughness from experiment to experiment. A $79 \mu m$ diameter NiCr wire filament, is positioned at the desired nucleation site and sandwiched between the two compressed Homalite quadrilateral test sections as shown in Fig. 11. The wire is seated within the hole formed by a matching pair of semi-circular channels so as to avoid any mechanical interference with the frictional interface when the plates are compressed.

The two quadrilateral test sections are brought into contact and compressed together as shown to create a frictional fault, which is inclined at an angle α with respect to the horizontal axis. A static compressive stress P, applied to the top and bottom surfaces of the square test specimen assembly translates into a normal traction

$$\sigma_{yy}^0 = P \cos^2 \alpha \tag{57}$$

resolved shear stress traction

$$\sigma_{yx}^0 = P \sin \alpha \cos \alpha \tag{58}$$

along the inclined frictional interface, which mimic tectonic stresses imposed on a strike-slip frictional fault within the Earth's crust. Interfacial sliding is prevented by virtue of the fact that the resolved shear stress does not exceed the peak (static) frictional strength $\tau_p = f_s \sigma_{yy}^0$ of the interface, where f_s represents the static coefficient of friction. A specimen fault angle $\alpha < 0$, measured with respect to the horizontal axis, assures that once nucleated, a right-lateral rupture will propagate along the frictional fault in response to the applied far field stress.

A dynamic rupture is nucleated with the aid of an electrical triggering circuit as depicted in Fig. 11. Electrical charge stored within a capacitor bank is dumped to ground and forced to pass the NiCr wire. The thin wire filament is unable to sustain the high current and is
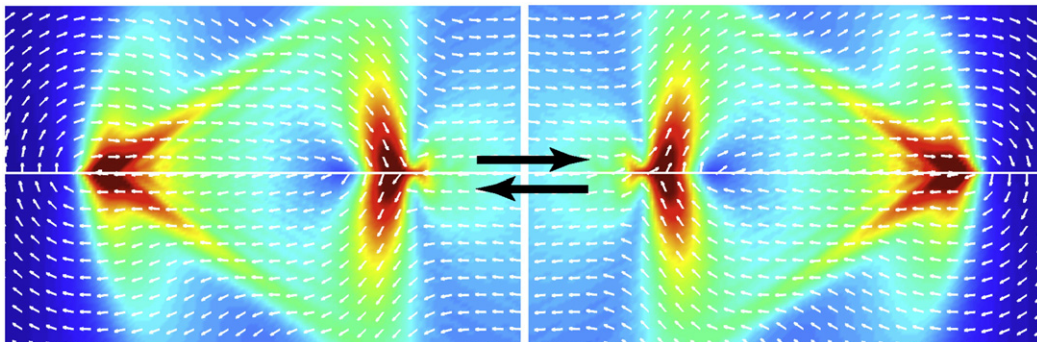

Fig. 10. Sense of particle motion for a spontaneous right-lateral supershear rupture. The contour plot shows the magnitude of the velocity field and the vectors show only the sense of motion.
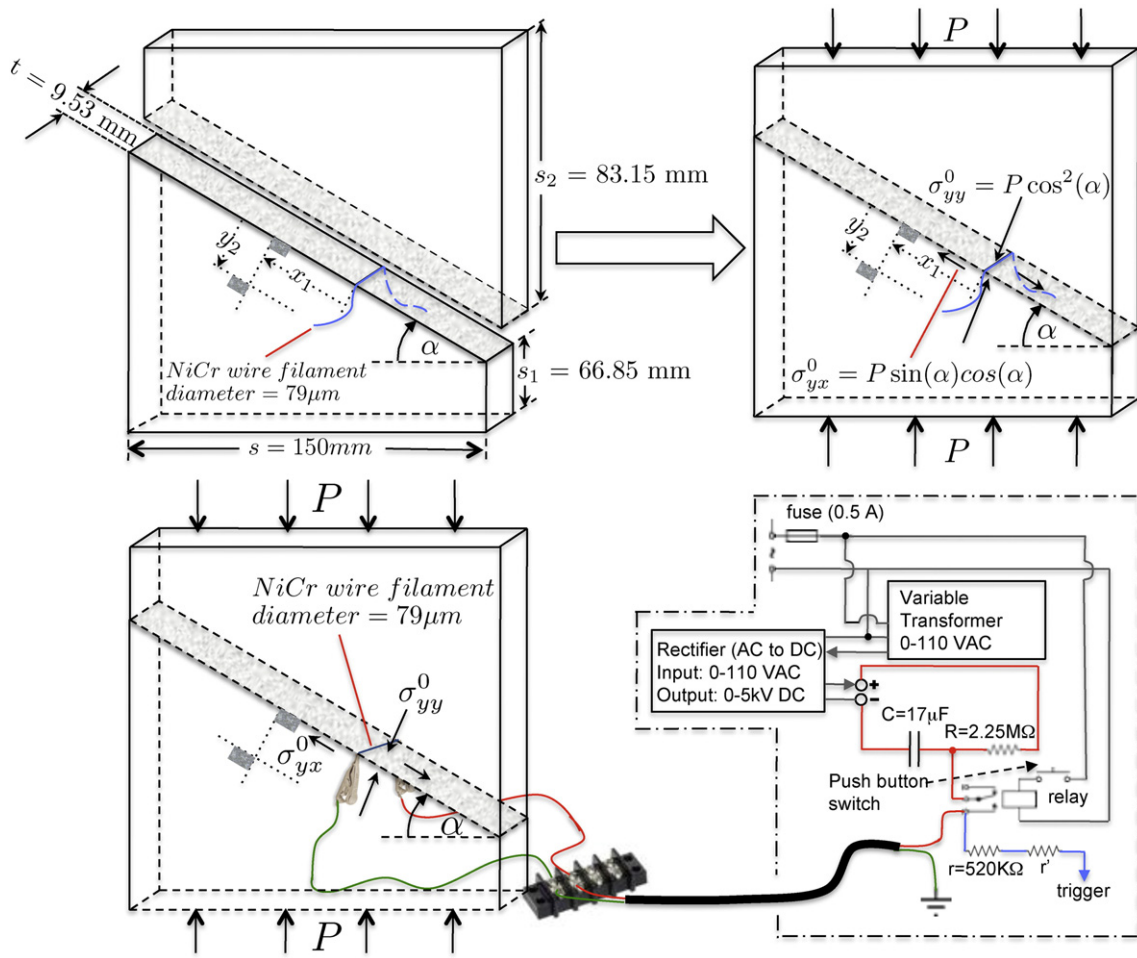
Fig. 11. Schematic of Laboratory Earthquake test specimen geometry, loading and nucleation scheme.

rapidly disintegrated. The resulting plasma discharge reduces the local normal traction (and thus the local static frictional strength) along the wire channel such that the applied shear traction σ_{yx}^0 becomes momentarily larger than the reduced frictional strength. The event induces a localized slip of the interface and the subsequent nucleation of a bi-lateral mode II rupture that propagates along the frictional fault. A second output signal, derived from the same circuit in the form of a 5V step with sub-microsecond rise time, is used to simultaneously trigger measurement diagnostics such as a digital oscilloscope and high speed gated-intensified CCD cameras.

3.1. Photoelasticity and high speed digital photography for spatially resolved, whole field imaging

The stress-birefringent property of Homalite-100 enables the application of Photoelastic interferometry in conjunction with high speed digital photography for full field imaging of a dynamic event with high spatial resolution. A pictorial overview of the current laboratory earthquake experiment, in its current form, including a detailed schematic of the photoelastic optical interferometer arrangement is depicted in Fig. 12. A continuous wave solid state laser emits a vertically polarized laser beam of wavelength $\lambda = 532nm$, which is expanded to a nominal beam diameter $\approx 145mm$. The linearly polarized light beam is converted to a right hand (RH) circularly polarized state, then transmitted through the test object, and finally processed by a left hand (LH) circular polarizer as shown. While mechanically unstressed, the Homalite test specimen remains optically isotropic and the polarization state of the transmitted beam remains unperturbed. The transmitted light field is then

completely suppressed by the LHCP and the resulting image is void of any interference fringes. The optical configuration is thus commonly referred to as a dark field polariscope arrangement. When mechanically stressed, the H-100 test specimen becomes optically anisotropic and the transmitted light field is no longer circularly polarized. The dark field image is then transformed into an interference pattern with bright and dark fringes corresponding to isocontours of maximum shear stress within the plane of the test specimen.

The "stress optic law" relating the relative change in the maximum shear stress ($\Delta\tau_{max}$) to a corresponding fringe order N in the photoelastic pattern is given by

$$\Delta\tau_{max} = \frac{f_\sigma}{2h}N, \tag{59}$$

where h corresponds to the H-100 test specimen thickness and $f_\sigma = 23.03kN/m$ for H-100 (Kobayashi, 1993). The "fringe counting relationship" given by Eq. (59) reveals how photoelastic fringes directly correspond to isocontours of maximum shear stress. Note that there is no reference to the principle angle and that the interpretation of a photoelastic fringe pattern using Eq. (59) must be conducted with the understanding that dark field fringes correspond to isocontours of maximum shear stress in magnitude only.

A 1000 mm f/6.9 plano-convex field lens collects the expanded light field and focuses it down into an array of camera lenses mounted within a baffled tube assembly as depicted in Fig. 12. A 50/50 non-polarizing beam splitter divides the imaging path and directs each laser beam into a Cordin model 220 ultra-high speed camera as
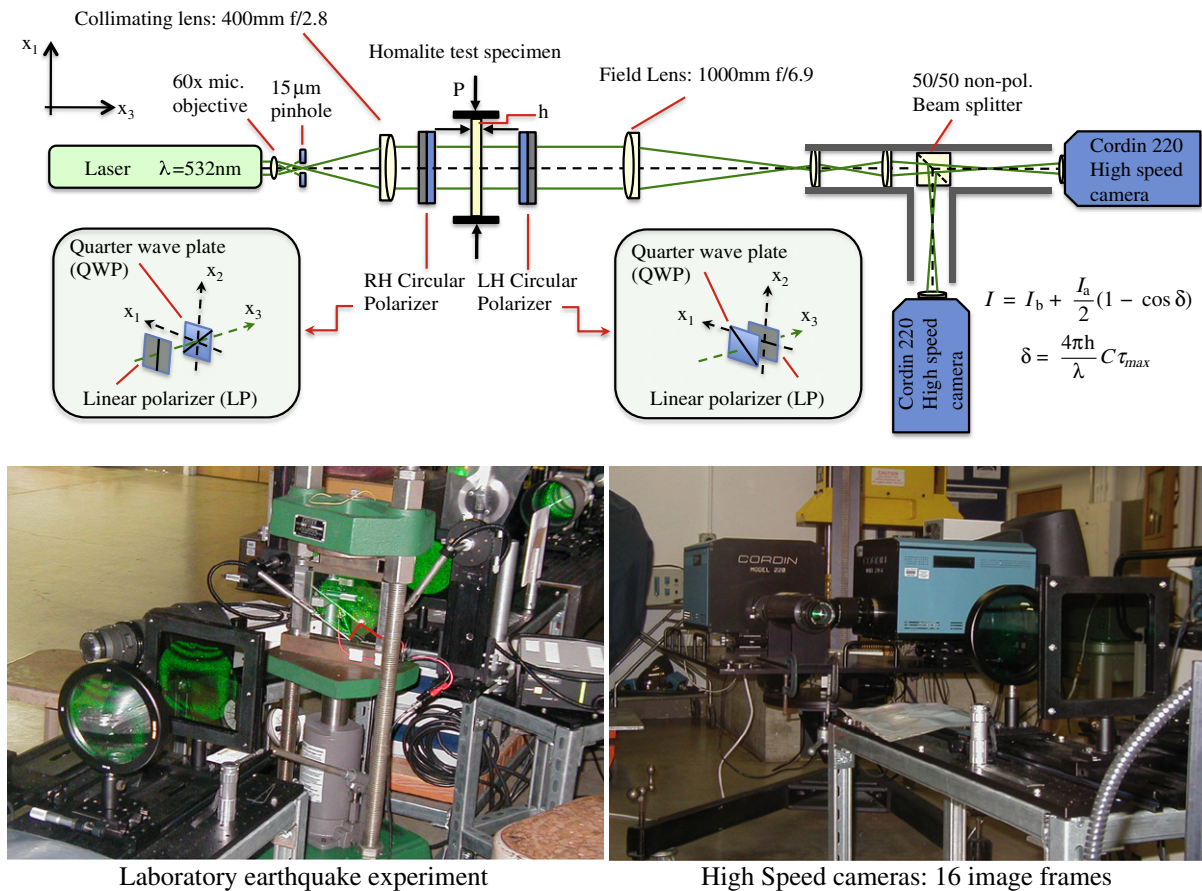
Fig. 12. Laboratory earthquake experiment featuring photoelastic interferometry in conjunction with high speed photography for full field imaging of a dynamic rupture with high spatial resolution.

shown. The imaging beams are split yet again by internally mounted pellicle beam splitters within each camera and directed to a sharp focus onto 8 individual 767×574 pixel, gated-intensified, progressive scan CCD sensors. Each camera thus acquires a total of 8 images in a single shot event and the two cameras are sequentially triggered to generate a total of 16 high resolution whole-field images. Typical inter-frame times in a laboratory earthquake experiment range anywhere from $1-4\mu s/frame$ with $50ns$ of photon integration time per image frame.

3.2. Fiber optic heterodyne interferometers for continuous particle velocity measurements

Heterodyne laser interferometers, first introduced by Lykotrafitis and Rosakis (2006) in dynamic shear crack investigations and then later applied by Lu et al. (2007), Rosakis et al. (2007) in laboratory earthquake experiments, are now routinely applied to obtain continuous, high bandwidth measurements of fault-normal (FN) and fault-parallel (FP) particle velocity particle velocity records at fixed locations on the surface of a test specimen as a sub-Rayleigh or supershear rupture sweeps along the frictional fault. FN and FP velocity records obtained in this manner are thus analogous to ground motion measurements recorded by seismograph stations on the surface of the Earth in the immediate neighborhood of an active fault.

The pair of red line segments in the left hand image of Fig. 12 highlight the Helium Neon laser beams that are focused at nearly grazing incidence to a fixed point of interest on the surface of the test specimen. Focusing fiber optic probes, with a continuously adjustable working distance, are attached to stainless steel periscope extensions as depicted in the image. Miniature reflectors at the tip of each

periscope extension, inclined at 45° to the optical axis, direct the laser beam to focus over an approximately $100\mu m$ diameter spot at the corner of a thin square strip of retro reflective tape adhered to the specimen surface. Scattered light, directed back along the incident light path, is collected by each probe and directed back to a Polytec model OFV-511 heterodyne interferometer where the light is optically interfered. Fig. 13 provides a detailed schematic representation of the heterodyne laser interferometer configuration adopted in the laboratory earthquake experiment. The resulting signal frequency f_s produced by the interfering beams is given by

$$f_s = f_b + f_d \tag{60}$$

where f_b is a constant signal frequency of 40 MHz introduced by a Bragg cell in the reference arm of the interferometer and f_d is the Doppler frequency shifted contribution given by

$$f_d = -\frac{2\dot{u}_i(t)}{\lambda}cos\,\alpha. \tag{61}$$

Here $\lambda = 632.8nm$ is the HeNe laser wavelength, $u_i(t)$ ($i = 1,2,3$) corresponds to the surface displacement component of interest, and α represents the angle between the optic axis as defined by the focused laser beam and a unit vector parallel to the particle motion component of interest. The $cos\alpha$ factor accounts for the effect of non-normal or non-grazing incidence. In most cases the optical axis defined by the focused laser beam is within $5° - 10°$ of the targeted coordinate direction, in which case $cos\alpha \rightarrow 1$. As the specimen surface displaces, the resulting signal frequency f_s is either perturbed above or below the reference frequency f_b, depending upon the sign of u_i.
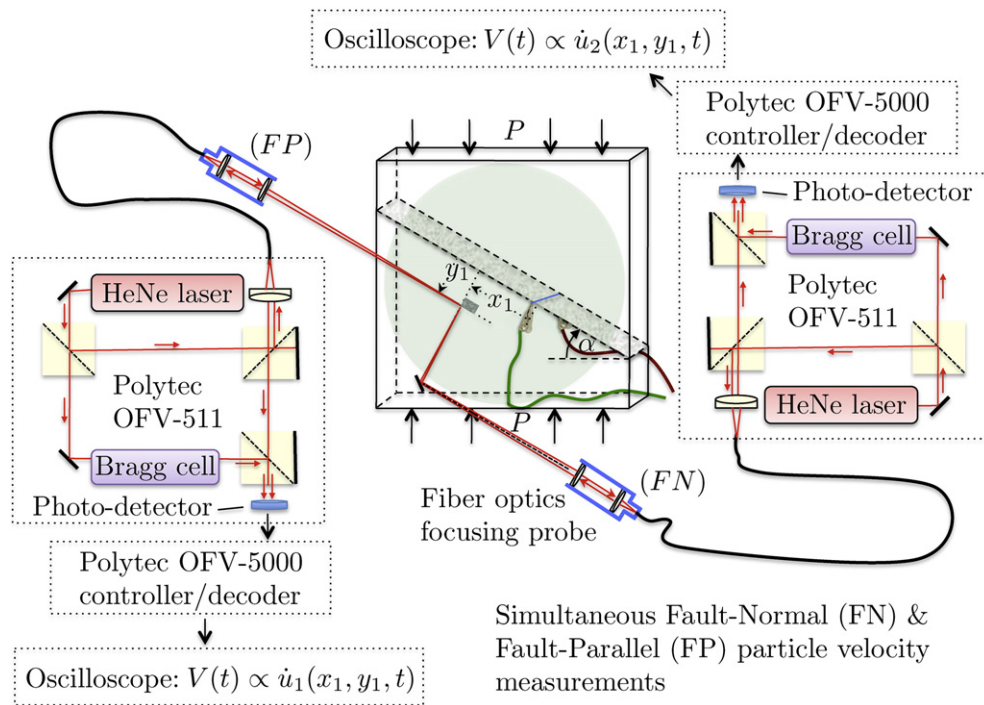
Fig. 13. Fiber optic heterodyne laser interferometer for continuous particle velocity measurements with high temporal resolution at a discrete positions on the surface of a laboratory earthquake test specimen.

Proper frequency demodulation of the heterodyne interferometer signal frequency then leads to a direct and unambiguous measure of particle velocity. The interferometer signal is processed by a Polytec OFV-5000 controller featuring a $1.5MHz$ bandwidth model VD-02 velocity decoder capable of tracking particle velocities up to $10m/s$ with a resolution of $0.15m/s$. A continuous particle velocity record in the form of an analog voltage-time record, is then output from the controller and directed to a Tektronix DPO3034, 300 MHz analog bandwidth oscilloscope, where the signal is sampled at $2.5Gs/s$ ($0.4ns/datapoint$). The acquired traces are then converted to particle velocity records through a calibrated scaling factor ($1V = 1m/s$).Note that the $1.5MHz$ bandwidth specification for the VD-02 applies to the analog bandwidth of the final processed particle velocity record as captured by the oscilloscope. A bandwidth limit of $1.5MHz$ translates into a minimum resolvable particle velocity rise time of $\tau = 0.2\mu s$.

Three velocity measurement schemes commonly adopted in laboratory earthquake investigations are depicted in Fig. 14. The light green circle in each figure represents the expanded laser beam, used for photoelasitc imaging, which is simultaneously transmitted through the H-100 test specimen in order to obtain synchronized whole field images of the event. Fig. 14a depicts the paired FN particle velocity measurement scheme. In this configuration, a pair of fiber optic probes are oriented so as to obtain simultaneous FN particle velocity records at two independent measurement stations, one of which is located on the fault and a second which is located at an off-fault station along a line oriented normal to the fault as shown. The paired FN particle velocity measurement scheme is particularly useful for investigating the attenuation of sub-Rayleigh ground motion where $\dot{u}_2(t)$ is expected to be the dominant ground motion component. Fig. 14b depicts the paired fault parallel particle velocity measurement scheme. In this configuration, a pair of fiber optic probes are oriented so as to obtain simultaneous fault parallel particle velocity records at two measurement stations, one of which is located on the fault and a second which is located at an off-fault station along a line oriented normal to the fault as shown. The paired fault parallel scheme is used to investigate the attenuation of supershear ground motion where u_1 is expected to be the dominant particle velocity component. The third fiber optic probe configuration

depicted in Fig. 14c (same as depicted in 12 and 13) corresponds to the case where both a FP and FN particle velocity record are simultaneously acquired at a fixed location on the surface of the test specimen. This configuration is in many ways analogous to a seismograph station on the surface of the Earth, which is situated close to an active strike slip fault. The combined FP/FN measurement scheme has been successfully applied to the investigation of both sub-Rayleigh and supershear ruptures in order to identify the dominant motion component in each respective case in addition to capturing any other unique ground motion signatures that accompany or trail the primary rupture front. Other combinations of paired particle velocity measurements may also be configured depending upon the design and objectives of a given experiment.

Fig. 14d and e depict two velocity measurement station configurations, which may be adopted when working with either of the paired particle velocity measurement configurations depicted in Fig. 14a and b. Each configuration provides a unique approach for investigating the attenuation of particle velocity as a function of the FN distance (y_2). The station configuration depicted in Fig. 14d corresponds to the most commonly used configuration whereby the measurement station locations are aligned along a line drawn normal to the fault. This configuration is particularly suited for investigating the attenuation of sub-Rayleigh rupture field as a function of FN distance. The configuration in Fig. 14e depicts a pair of measurement stations oriented along a line drawn normal to the anticipated shear Mach front. The spirit of the latter configuration centers around the notion that the information contained in the FP record at an off-fault station is propagated to this location by the shear wave radiation emitted from rupture tip as it swept the corresponding on-fault location. Attenuation measurements conducted using the latter station configuration will thus naturally exclude the effects associated with the rupture velocity history.

3.3. Estimation and control of supershear transition length in laboratory earthquake experiments

Burridge (1973) was the first to theoretically describe the conditions under which a plain-strain, self-similar mode II crack can
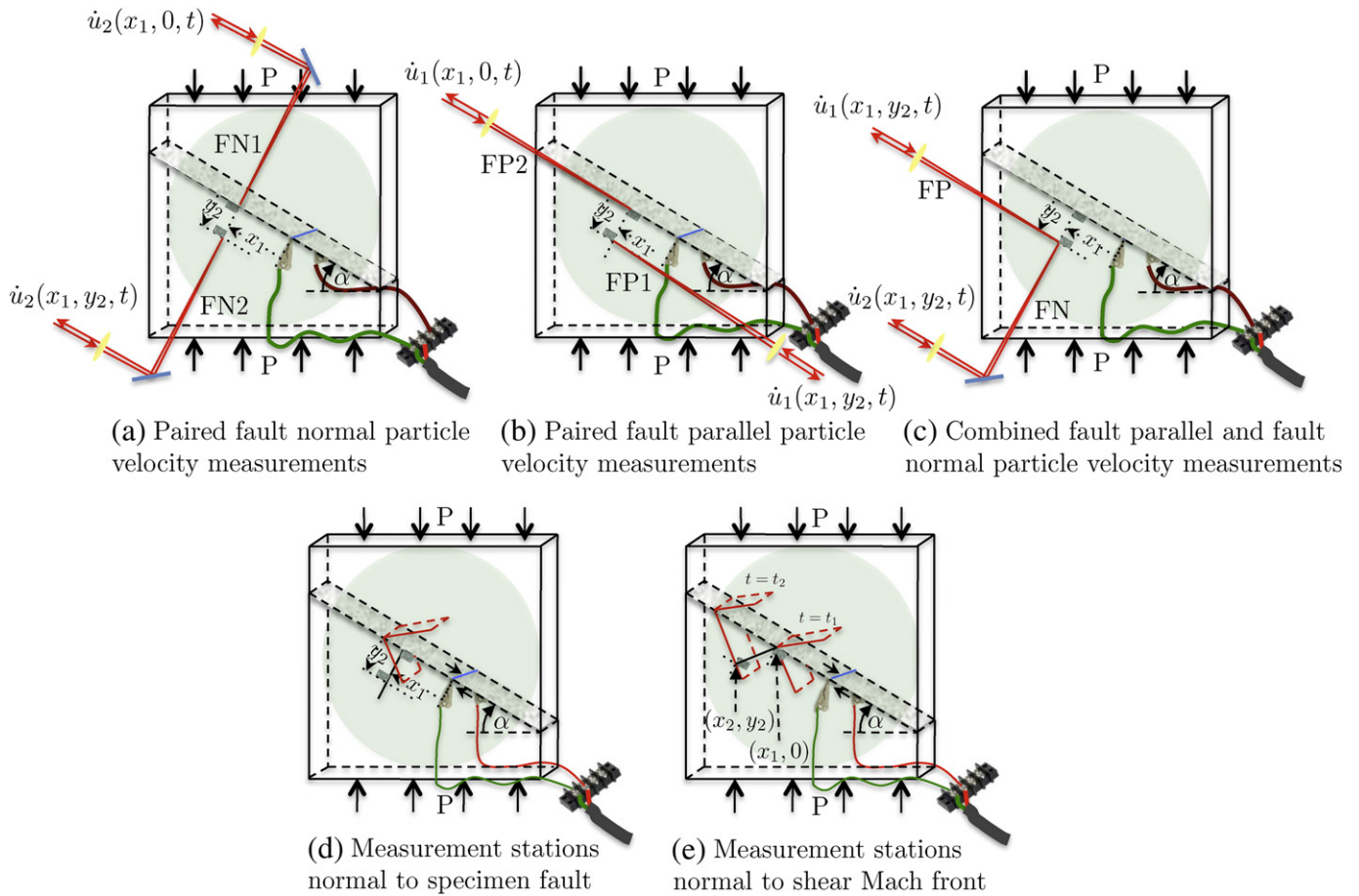
(a) Paired fault normal particle velocity measurements

(b) Paired fault parallel particle velocity measurements

(c) Combined fault parallel and fault normal particle velocity measurements

(d) Measurement stations normal to specimen fault

(e) Measurement stations normal to shear Mach front

Fig. 14. Particle velocity measurement configurations adopted in laboratory earthquake experiments.

propagate in the supershear regime. Burridge's original derivation assumed a Coulomb friction relation for the slip zone just ahead of the crack tip but neglected to account for the effects of inelastic (cohesive) energy losses at the crack tip. The analysis did however successfully predict the existence of a peak in the shear stress field, situated on the S-wave and just ahead of the primary crack front, that could potentially overcome the critical (frictional) shear stress level and initiate secondary slip at that location. According to the model, the subsequent merger of the primary rupture traveling at the Rayleigh-wave speed with the newly formed secondary rupture front, propagating at or greater than the S-wave speed, leads to the formation of an supershear rupture front.

Andrews (1976) followed with numerical finite difference calculations that successfully simulated the sub-Rayleigh to supershear transition, resulting from a merger of primary and secondary rupture fronts, in a manner consistent with Burridge's original predictions (Burridge, 1973). The numerical model featured a linear slip weakening friction law, graphically depicted in Fig. 15, which provided both a finite stress criterion $\tau \leq \tau_P$ and accounted for fracture energy G_c, given by

$$G_c = \frac{1}{2}\left(\tau_p - \tau_r\right)D_c \qquad (62)$$

which distinguished the analysis from the earlier analytical treatment adopted by Burridge. The sub-Rayleigh to super-shear transition, originally theorized by Burridge and later demonstrated and further interpreted by Andrews, is commonly referred to as the Burridge–

Andrews mechanism. The persistence of this mechanism over an astonishing range of length scales is discussed by Rosakis (2002). Andrews (1976) further examined the sub-Rayleigh to supershear transition and reasoned that the transition length L, corresponding to the distance over which a sub-Rayleigh rupture transitions into a supershear rupture, is related to the critical (plane strain) crack half-length L_c

$$L_c = \frac{\mu\left(\tau_p - \tau_r\right)D_c}{\pi(1-\nu)\left(\sigma_{yx}^0 - \tau_r\right)^2} \qquad (63)$$

measured from the epicenter, where ν is Poisson's ratio, μ is the shear modulus value, and D_c corresponds to the critical slip weakening distance.

It is easily shown that the normalized quantity L_c/L is equivalent to the energy absorbed by the rupture front to the amount of available strain energy which has been released to propagate the crack to a new length L (Andrews, 1976). Andrews incorporated these points and summarized his findings by plotting the dependence of L_c/L on the seismic S-ratio

$$S = \frac{\tau_p - \sigma_{yx}^0}{\sigma_{yx}^0 - \tau_r} \qquad (64)$$

Points derived from numerical trials define the boundaries of a transitional region, which divide the sub-Rayleigh regime on the right
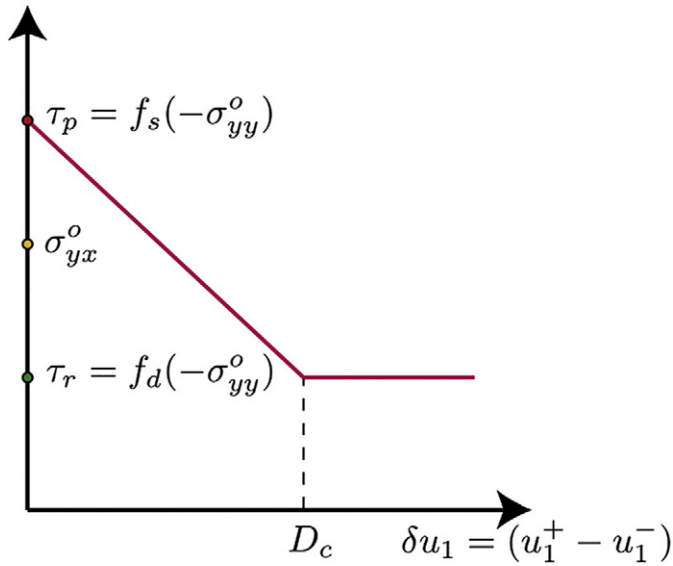
Fig. 15. Linear slip-weakening friction law.

from the super-shear regime on the left. Andrews result can be restated as

$$L = F(S)L_c = 9.8(1.77 - S)^{-3}L_c \qquad (65)$$

(Xia et al., 2004) where the function $F(S)$ is numerically obtained from Andrews plot. The unique point $S \approx 1.77$, represents an upper value for the seismic S ratio, where $L \to \infty$, beyond which a sub-Rayleigh rupture cannot possibly transition into the super-shear regime. The lower limit $S \to 0$, equivalent to $\sigma_{yx}^0 \to \tau_p$, corresponds to a lower bound for the transition length given by $L \approx 1.77L_c$.

Original laboratory earthquake experiments conducted by Xia et al. (2004), Rosakis et al. (2007) provided the first direct evidence of the sub-Rayleigh rupture to supershear rupture transition through high speed photoelastic images. Image analysis revealed that the transition length L exhibited a faster decay with increasing uniaxial pressure P, than the expected $L \propto P^{-1}$ dependence, assuming Andrews (1976) analysis was applicable to the laboratory data. The observed discrepancy was first attributed to a pressure dependency of the critical slip weakening distance D_c in the slip-weakening friction law that was unaccounted for in Andrews model. Xia et al. (2004), Rosakis et al. (2007) combined results from rock friction experiments obtained by Ohnaka (2003) with a simple asperity-contact based frictional model to show that $D_c \propto P^{-1/2}$. Specifically,

$$D_c = C \left(\frac{\tau_s - \tau_r}{\tau_r}\right)^M \sqrt{H}a_0 \cos \alpha P^{-1/2} \qquad (66)$$

where C, M are constants, H is the hardness of the material (defined as the ratio of the total normal force to the actual contact area), and a_0 represents the mean radius of contact asperities (Xia et al., 2004).

Assuming plane stress loading conditions in the laboratory earthquake test specimen leads to a modified expression for the critical crack half-length given by

$$L_c = \frac{\mu(1 + \nu)(\tau_p - \tau_r)D_c}{\pi(\sigma_{yx}^0 - \tau_r)^2} \qquad (67)$$

Before continuing with the modified transition length derivation, it is instructive to note how the critical crack half-length relation Eq. (67) reinforces the use of Homalite (or other brittle, mildly rate sensitive polymeric materials) as a model material of choice in the

laboratory earthquake experiment, as opposed to using test specimens fashioned from crustal rock material. The critical crack half-length relation given by Eq. (67), and thus the supershear transition length, are seen to scale in direct proportion to the shear modulus of the surrounding medium. Homalite-100 has a shear modulus of $\mu = 1.7GPa$ (Dally and Riley, 2005), which is at least 30× less than the shear modulus value of crustal rock. Experiments have demonstrated that typical H-100 supershear transition lengths generally range from $10mm - 100mm$ depending upon test conditions and the nature of the investigation. Thus, assuming a similar critical slip weakening distance (D_c) between H-100 and crustal rock, a sub-Rayleigh rupture nucleated in a rock specimen would therefore require a supershear transition length at least 30× greater ($0.3m < L < 3m$) than required with H-100 test specimens. The use of rock specimens in the current laboratory earthquake loading arrangement is therefore somewhat impractical at this time as it would necessarily require considerably larger (and far more massive) test specimens compared to the current $150mm \times 150mm$ Homalite-100 test specimen dimensions.

Returning now to the transition length discussion, we can substitute the pressure dependent relation for Eq. (66) into Eq. (67), while observing that the supershear transition length L should scale with L_c and invoking Eqs. (57), (58), to obtain a modified transition length relation given by

$$L = F(s)\left[\frac{\mu(1 + \nu)C\sqrt{H}a_0 \cos \alpha}{\pi(\sin \alpha - f_d \cos \alpha)^2}\right] \times \left(\frac{f_s - f_d}{f_d^{M-1}}\right)^{M+1} P^{-3/2} \qquad (68)$$

A detailed derivation of the revised transition length expression Eq. (68) is given in (Rosakis et al., 2007), where an analytical approximation of the function $F(s)$ of the seismic S-ratio is provided. It was also shown that Eq. (68) is in good agreement with measured supershear transition lengths obtained through laboratory earthquake experiments (Xia et al., 2004) with a_0 as a fitting parameter.

Lu et al. (2008) followed by numerically examining the effect of the dynamic rupture initiation procedure and fault friction on supershear transition using a plane-stress model with an interface governed by linear slip weakening friction. A rupture initiation procedure that mimicked the dynamic nature of the discharging NiCr wire filament was achieved by reducing the normal stress over a part of the interface for a given time. Results demonstrated that dynamic rupture initiation procedure can, at times, significantly shorten the supershear transition length observed in experiments, compared to those predicted through the quasi-static rupture initiation process. Moreover, it was further determined that in some cases, the dynamic initiation procedure changes the very mode of transition, causing a direct supershear transition at the tip of the main rupture instead of the Burridge-Andrews, mother-daughter mechanism. Last, but not the least, it is also possible, and even likely, based on the study conducted by Lu et al. (2007), that the interface friction is better described by a rate and state-dependent law with significant rate-dependence at high slip rates rather than a linear slip-weakening law used in this work. The effect of such a law on transition length will be explored in future studies.

3.4. Control of rupture speed regime in laboratory earthquake experiments

An alternative form for the seismic S-ratio, strictly applicable to the laboratory earthquake loading configuration, is given by

$$S = \frac{f_s - \tan \alpha}{\tan \alpha - f_d} \qquad (69)$$

As noted by Andrews (1976), a seismic S-ratio $S < 1.77$ assures that a sub-Rayleigh rupture will transition to supershear rupture.

Assuming that this condition is satisfied in a laboratory earthquake experiment, the supershear transition length may then be controlled by varying the specimen fault angle α and the applied static compressive stress P, in accordance with Eq. (68), assuming fixed values for the static and dynamic frictional coefficients f_s, f_d, elastic constants μ, ν and contact asperity parameters C, M, H, a_0. The value of the specimen fault angle in a typical laboratory earthquake experiment ranges between $20° < \alpha < 30°$. Specimen fault angles less than $20°$ require too much static pressure, which may induce buckling of the H-100 plate assembly whereas specimen faults oriented at angles greater than $30°$ are prone to slip under the applied static load. Taking $f_s = 0.6$, $f_d = 0.2$, as representative values for the static and dynamic frictional coefficients leads to $0.06 < S < 1.44$. The sub-Rayleigh to supershear transition criterion $S < 1.77$ is evidently satisfied over the entire range of specimen fault angles thus implying that a sub-Rayleigh rupture will invariably transition into a supershear rupture. Whether or not a sub-Rayleigh rupture will transition to a supershear rupture for upper limiting values of the seismic S-ratio $S \to 1.44$ is dictated by the physical dimensions of the test specimen and the available propagation distance L, measured from the nucleation site to the edge of the specimen fault. Laboratory earthquake rupture propagation scenarios are therefore controlled by either fixing the fault angle α and varying the static pressure P or vice versa so as to modulate L in relation to L. The condition $L > L$ and Eq. (68) thus assure that a nucleated rupture will remain within the sub-Rayleigh rupture speed regime for the duration of the experiment whereas $L < L$ assures that a sub-Rayleigh to supershear transition will occur between the rupture nucleation site and the edge of the frictional fault. The ability to adjust the supershear transition length in the laboratory earthquake experiment thus provides a versatile test platform for investigating various earthquake scenarios and frictional

faulting processes involving both types of dynamic ruptures. The image sequence in Fig. 16 demonstrates the sub-Rayleigh (SR) to supershear (SS) transition as captured through high speed photography of photoelastic fringe patterns. Fig. 16a corresponds to a time $t = 25\mu s$ after trigger. The leading P-wave front is just shy of sweeping the position markers with noted lower right and left hand corners situated at $(-55,0) mm$ and $(-55,16) mm$, measured with respect to the rupture nucleation site. The sub-Rayleigh (SR) rupture corresponds to the concentrated fringe pattern sitting just behind the S-wave front. Note the continuous dark fringe loop extending out beyond the SR rupture, which closes back on itself at the SR rupture tip. The onset of a SR to SS transition is captured in Fig. 16b, acquired at $t = 33\mu s$, as revealed by an apparent discontinuity in the leading fringe loop. The first hint of a Mach cone is revealed in Fig. 16c, acquired at $t = 37\mu s$, by the dark triangular-shaped fringe seen extending out beyond the SR rupture front. Fig. 16d, acquired at $t = 41\mu s$, displays a sharp Mach cone stemming from a supershear rupture tip, which is just crossing the on-fault position marker situated at $(-55,0) mm$. The two final image frames show the shear Mach fronts to continue to grow in size as the supershear rupture propagates toward the edge of the fault. Frame by frame analysis of the supershear rupture tip position along with measurement of the Mach cone angles in the photoelastic image sequence confirms a rupture speed within the stable rupture speed regime ($\sqrt{2}C_s < V_r < C_p$). A secondary rupture propagating at the Rayleigh wave speed in Homalite-100, herein referred to as a trailing Rayleigh disturbance, is also revealed by the tight fringe concentration, which trails in the wake of the supershear rupture. Note how the supershear rupture is clearly outrunning the trailing Rayleigh disturbance as revealed by the increased distance between the two features in each successive image frame.
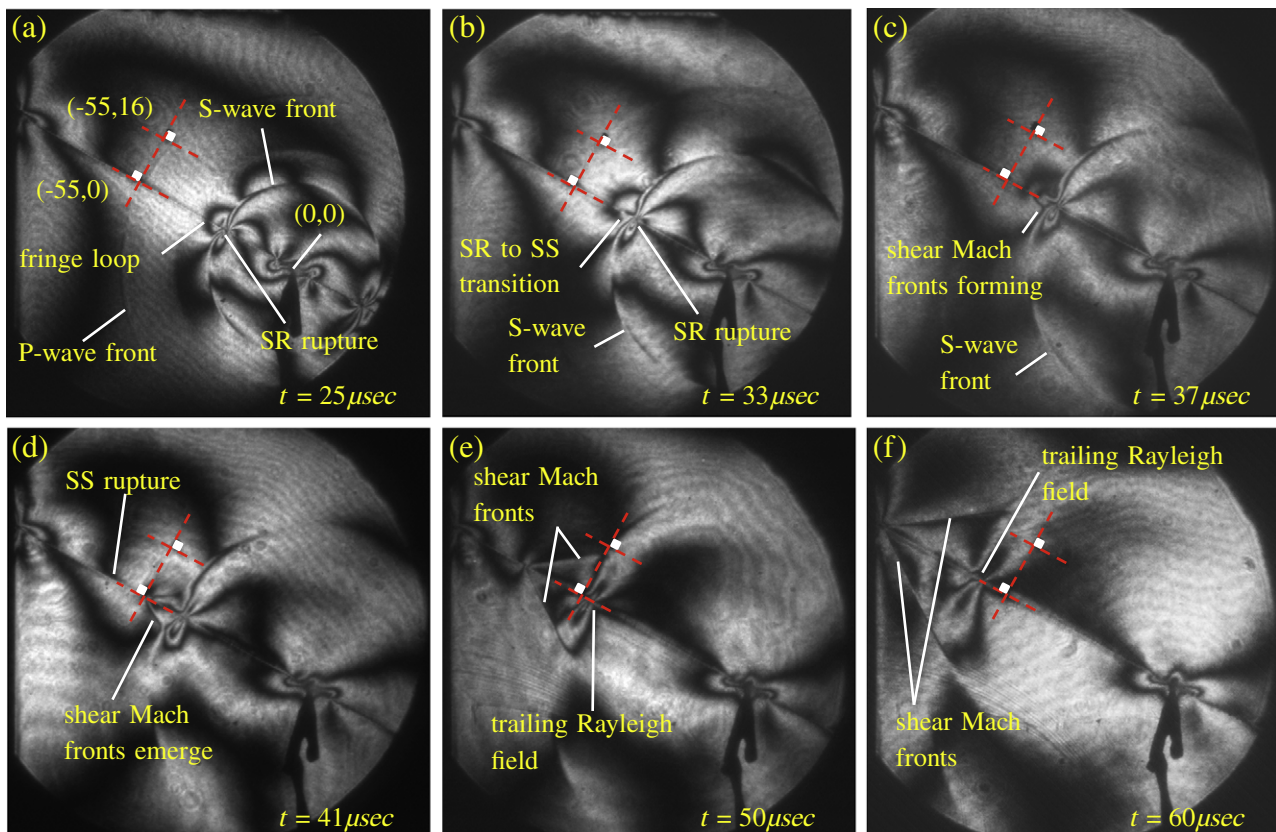

Fig. 16. Sequence of photoelastic images revealing sub-Rayleigh to supershear transition.

3.5. Experimental investigation of particle velocity field attenuation: comparison between a sub-Rayleigh and a supershear rupture

The left hand plot in Fig. 17 depicts a pair of FN particle velocity records resulting from the passage of a sub-Rayleigh rupture. The two FN velocity records were simultaneously acquired at $(-55,0)mm$ and $(-55,10)mm$ using the paired measurement station scheme featured in Fig. 14a. The black triangles situated along the time axis in each plot correspond to the 16 synchronous photoelastic image frames acquired during the same experiment. Analysis of the rupture position in the photoelastic image sequence reveals a rupture speed of $1.12mm/\mu s$ ($0.87C_s$). Each signal exhibits a highly symmetric FN velocity pulse associated with passage of the sub-Rayleigh rupture with peak velocities registered at approximately $t = 54\mu s$ in each record. Note the 54% drop in the magnitude of the peak value of the off-fault record, registered only 10 mm from the corresponding on-fault station, which demonstrates the rapid attenuation of sub-Rayleigh ground motion with increased FN distance.

The supershear velocity record on the right features a pair of FP particle velocity signals that were simultaneously acquired using the paired measurement station scheme featured in Fig. 14b along with the measurement station configuration depicted in Fig. 14e. An off-fault record obtained at $(-72,24)mm$ is compared to an on-fault record at $(-55,0)mm$, situated $29.4mm$ away along a line drawn normal to the anticipated Mach front. The coordinate of the off-fault station was calculated based upon Mach angle measurements obtained from previous supershear experiments. The on-fault record (FP1) exhibits a sharp peak, coinciding with rupture arrival, approaching $\dot{u}_{1_{max}} \approx 7.6m/s$ in the neighborhood of $t = 36\mu s$. The corresponding off-fault record (FP2) displays a broadened peak, induced by passage of the leading dilatational field, approaching $\dot{u}_1 \approx 1.3m/s$ in the neighborhood of $t = 52\mu s$. This is quickly followed by a fairly sharp rise, attributed to the passage of the shear Mach front, leading to a second peak near $\dot{u}_{1_{max}} \approx 1.9m/s$ in the neighborhood of $t = 60\mu s$. The off-fault record (FP2) clearly demonstrates how a pronounced FP velocity jump is propagated out to a remote location by the supershear shear Mach front. This FP ground motion signature has been repeatedly observed at various measurement station locations in numerous supershear experiments. An off-fault counterpart to this particle velocity signature is not observed in sub-Rayleigh experiments. The paired supershear particle velocity records reveal a drop of nearly 75% in the peak magnitude of the FP component at the off-fault station with respect to the on-fault rupture source strength. Note however that the distance between the on and off-fault stations is almost $3\times$ greater than the corresponding distance in the sub-Rayleigh experiment. For proper consideration of attenuation of supershear velocity records one needs to separately account for the attenuation of the leading dilatational field and the shear Mach fronts. This is still work in progress and shall be addressed in future work.

Last but not the least we note how the magnitude of particle velocities obtained in typical laboratory earthquake experiments are comparable to the magnitudes obtained from near-field natural earthquake velocity records. We provide below a simple non-dimensional argument to explain this fact.

Based on the steady-state slip pulse models of Rice et al. (2005), Dunham and Archuleta (2005) the proper non-dimensionalized representation of the velocity field in a medium hosting such a slip pulse is given by

$$\frac{\mu \dot{u}}{\left(\tau_p - \tau_r\right)C_s} \equiv C\dot{u} = F(V_r/C_s, R/L) \tag{70}$$

where μ is the shear modulus, $\tau_p - \tau_r$ is the strength drop, $\dot{u}$ is the particle velocity, R/L is the ratio of the size of the process zone to slip pulse length and V_r/C_s is the rupture velocity scaled by the shear wave speed. In fact this is a universal feature which applies to all elastodynamic steady-state models independent of frictional or cohesive law used (e.g. Samudrala et al., 2002a). Consider that the typical value for the shear modulus of crustal rock is about 30 GPa. The corresponding value for Homalite is 1.7 GPa. If we assume Coulomb like friction ($\tau = f\sigma$, where f is the friction coefficient and σ is the normal stress) then at mid-seismogenic depths (around 7 km) σ is of the order of 100 MPa. Now if we assume $f_p = 0.6$ and $f_r = 0.2$ we get the strength drop to be of the order of 40 MPa for rock. This gives C for rock to be about 0.2. The strength drop in our experiments is about 8 MPa (assuming $\sigma = 20MPa$) giving a value of C close to 0.16, assuming R/L is similar for rupture in Homalite and crustal rock. Thus the velocity records obtained in Homalite should be comparable to the same in crustal rock.

4. Laboratory earthquakes: investigation of sub-Rayleigh and supershear ground motion signatures

4.1. Photoelastic image analysis of sub-Rayleigh and supershear ruptures

An image length scale calibration is established prior to each experiment by photographing a calibrated transparent length scale template, which is affixed to the surface of the H-100 test specimen. This procedure establishes a pixel to mm length scale conversion,
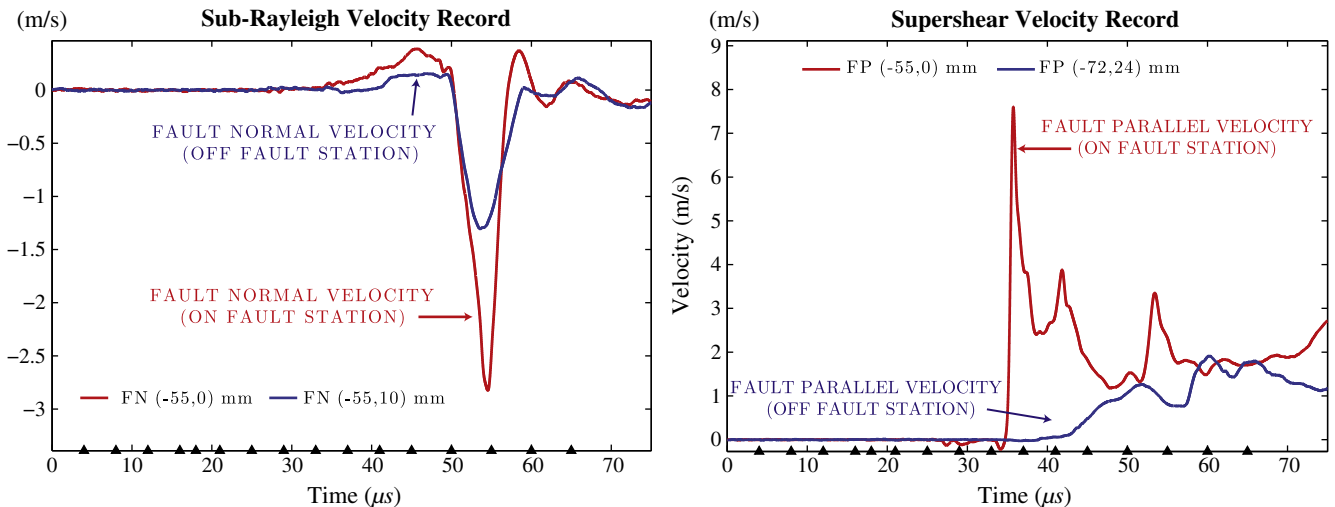

Fig. 17. Attenuation of sub-Rayleigh and supershear particle velocity field revealed through paired FN and paired FP particle velocity traces.

which is then used to measure wave speeds and rupture speeds when analyzing photoelastic images. The distance to a particle velocity measurement station, situated at the corner of the retro-reflector, is also accurately established using the same length scale calibration. The leading (P) and (S) wave fronts are revealed by sharp, concentric circular fringes in a photoelastic image. The center point of a concentric circle drawn over an S-wave or P-wave front establishes the coordinate (0,0) of the rupture nucleation site. The shear wave speed (C_s) and dilatational wave speed (C_p) are determined by tracking the radii of respective circular wave fronts. Wave speed values are precisely determined by taking the slope of a bestfit line passed through the position (wave front radius) vs. time datum obtained from a photoelastic image sequence. The time delay between the instrumentation trigger time and the onset of rupture nucleation is determined for each experiment by extrapolating the S-wavefront position versus time curve back to a time when the wave front radius $r = 0$. Application of this measurement technique to 50 independent laboratory earthquake experiments has yielded an average rupture nucleation delay time of 4.45 μs with a standard deviation of 0.33 μs. This time delay should be taken into account when attempting to estimate wave speeds or rupture speeds from the radius of a circular wave front or position of a rupture tip relative to the nucleation site in a photoelastic image. This factor must also be taken into account when establishing P and S wave arrival times in particle velocity records. Plots of the rupture tip position versus time in a photoelastic image sequence also lead to best fit slope estimates of sub-Rayleigh and supershear rupture speeds. An independent estimate of the supershear rupture speed may also be obtained by measuring the Mach angle and applying the Mach cone half-angle relation Eq. (1).

$$sin\,\theta = C_s\,/\,V_r \tag{71}$$

Table 2 lists the average shear and dilatational wave speed wave speed values for H-100 compiled from 50 independent laboratory earthquake experiments. The listed measurement uncertainty is a conservative estimate corresponding to the standard deviation of the 50 data points used to compile each of the listed values. The average sub-Rayleigh rupture speed V_r reported in the table was obtained from 47 of the 50 experiments.

4.2. Sub-Rayleigh and supershear particle velocity records resulting from a right-lateral rupture of an H-100 frictional fault, measured at a fixed location (−55.10)mm on the extensional side of a frictional fault

A series of laboratory earthquake experiments were conducted in order to examine, compare and contrast the rupture fields and ground motion signatures arising from sub-Rayleigh and supershear ruptures. The images highlighted in this section were obtained from two independent experiments, one of which resulted in a sub-Rayleigh rupture and a second experiment which resulted in a sub-Rayleigh to supershear transition. Sub-Rayleigh rupture experiments were conducted using a static pressure of $P = 12 MPa$ while supershear experiments were conducted with a static pressure of $P = 24 MPa$. Both experiments featured a specimen fault angle of $\alpha = -29°$, measured with respect to the horizontal. In each case the static loading arrangement and orientation of the specimen frictional interface resulted in a bilateral rupture with right-lateral slip of the frictional fault.

Table 2
Measured wave speed values and mean sub-Rayleigh rupture speed in Homalite™ H-100 obtained from laboratory earthquake experiments.

C_s (mm/μs)	C_p (mm/μs)	C_p/C_s	V_r/C_s ($V_r < C_R$)	V_r (mm/μs)
1.29 ± 0.02	2.61 ± 0.08	2.03 ± 0.05	0.892 ± 0.023	1.14 ± 0.03

Pairs of photoelastic Images and corresponding particle velocity traces resulting from sub-Rayleigh and supershear ruptures are shown side by side, as depicted in Fig. 18, so as to compare and contrast the two ruptures and highlight prominent features contained within the particle velocity signatures. Each of the images in a given image pair was acquired at the same time relative to trigger thus making it easier to conduct a frame by frame comparison of sub-Rayleigh and supershear ruptures. The field of view in both experiments was intentionally skewed to favor the left side of the test specimen in order to assure that the advancing rupture front would be clearly image while crossing the particle velocity measurement station on the extensional side of the fault located at (−55,10)mm.

The combined FN and FP particle velocity measurement scheme depicted in Fig. 14c was adopted in order to collect continuous FN and FP particle velocity records at this fixed location. A thin strip of retro reflective tape measuring approximately $3mm \times 3mm$ on a side is adhered to the surface such that its lower left corner was situated at (−55,10)mm. The blue and red arrows in the photoelastic images symbolize how the heterodyne laser beams used to collect the FP and FN velocity records were directed at nearly grazing incidence to the surface of the H-100 test specimen and focused to a spot size of approximately $100\mu m$ at the corner location. Synchronized photoelastic images provide a means of visualizing the location of the rupture front and other propagating field disturbances when interpreting the particle velocity records. The accompanying particle velocity traces display data out to approximately $4\mu s$ beyond the image frame time. A black triangle on the time axis of each particle velocity plot marks the time at which the image frame was acquired.

4.2.1. Analysis of photoelastic image sequence and particle velocity traces

The first pair of images depicted in Fig. 18 correspond to a time $t = 21\mu s$ relative to instrumentation trigger time. The antisymmetric fringe pattern, centered about the rupture nucleation site in each of the images, is the defining maximum shear stress field signature of a mode II rupture.

Propagating sub-Rayleigh (SR) ruptures traveling to the left and right in the left hand (SR) image are revealed by the tight concentration of fringes situated just behind the prominent circular S-wave front. Note as well the faint circular P-wave front which is also visible in the SR image. The green vertical line segments labeled (t_p) at $t = 25.5\mu s$ and (t_s) at $t = 47.0\mu s$ correspond to the anticipated arrival times of the leading P-wave and S-wave fronts at (−55,10)mm. Note that a rupture nucleation delay time of $\Delta t = 4.41\mu s$ was accounted for in establishing these wave arrival times. Corresponding FN and FP particle velocity traces remain flat up to this time since not even the leading P-wave front has crossed the measurement station.

The right hand (SS) image in Fig. 18 exhibits a denser antisymmetirc pattern about the rupture nucleation site resulting from a higher resolved shear traction and larger stress drop compared to the sub-Rayleigh rupture. A sub-Rayleigh to supershear transition is captured both to the right and left of the nucleation site, as revealed by the discontinuous leading fringe loops and the tight triangular concentration of fringes emerging just ahead of the circular S-wave front. FN and FP particle velocity traces remain flat up to this time since not even the leading P-wave front (seen as a very faint arc in the image) has crossed the measurement station.

Fig. 19, acquired at $t = 29\mu s$ displays a fully developed supershear rupture in the (SS) image, as revealed by the pair of shear Mach fronts that stem from the leading rupture tip and extend back toward the circular S-wave front. A concentrated dilatational field lobe is also revealed by the prominent fringes that loop out from the supershear rupture tip. The symmetric concentration of fringes situated in the wake of the shear Mach front (behind the S-wave front) corresponds to the photoelastic manifestation of the trailing Rayleigh disturbance.
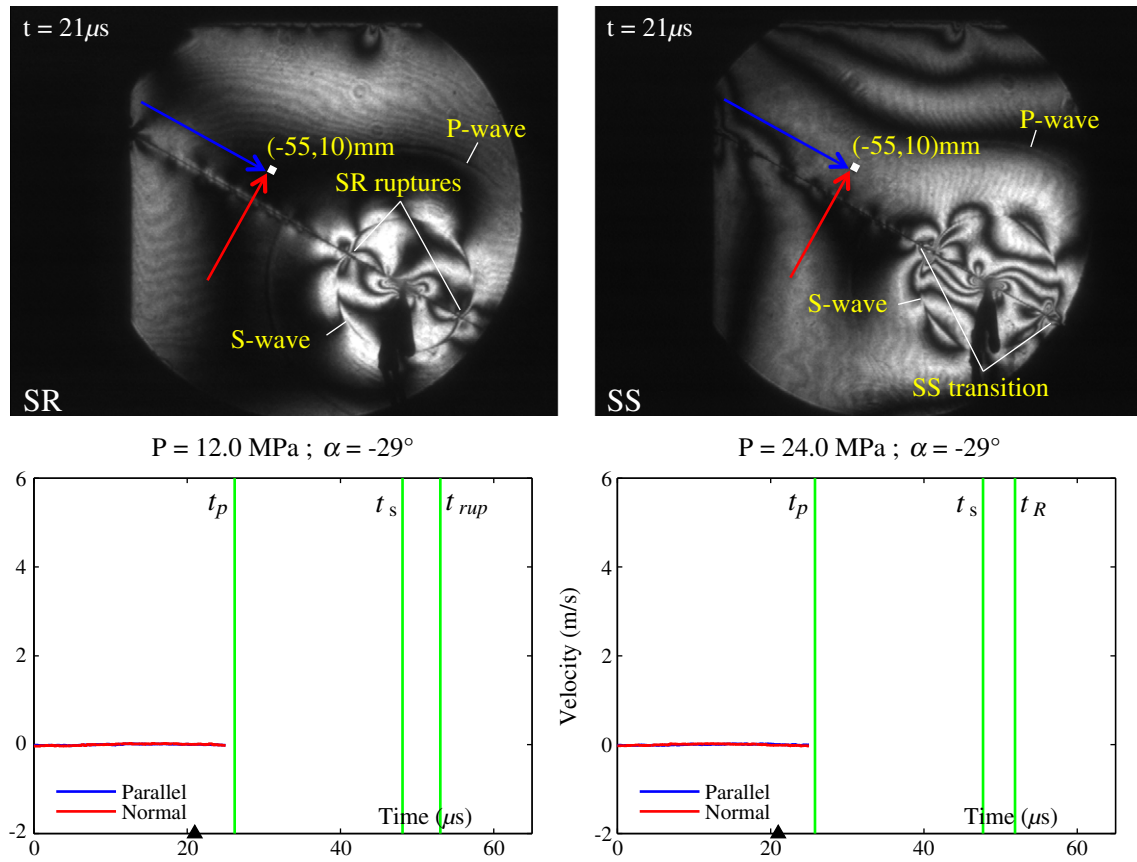
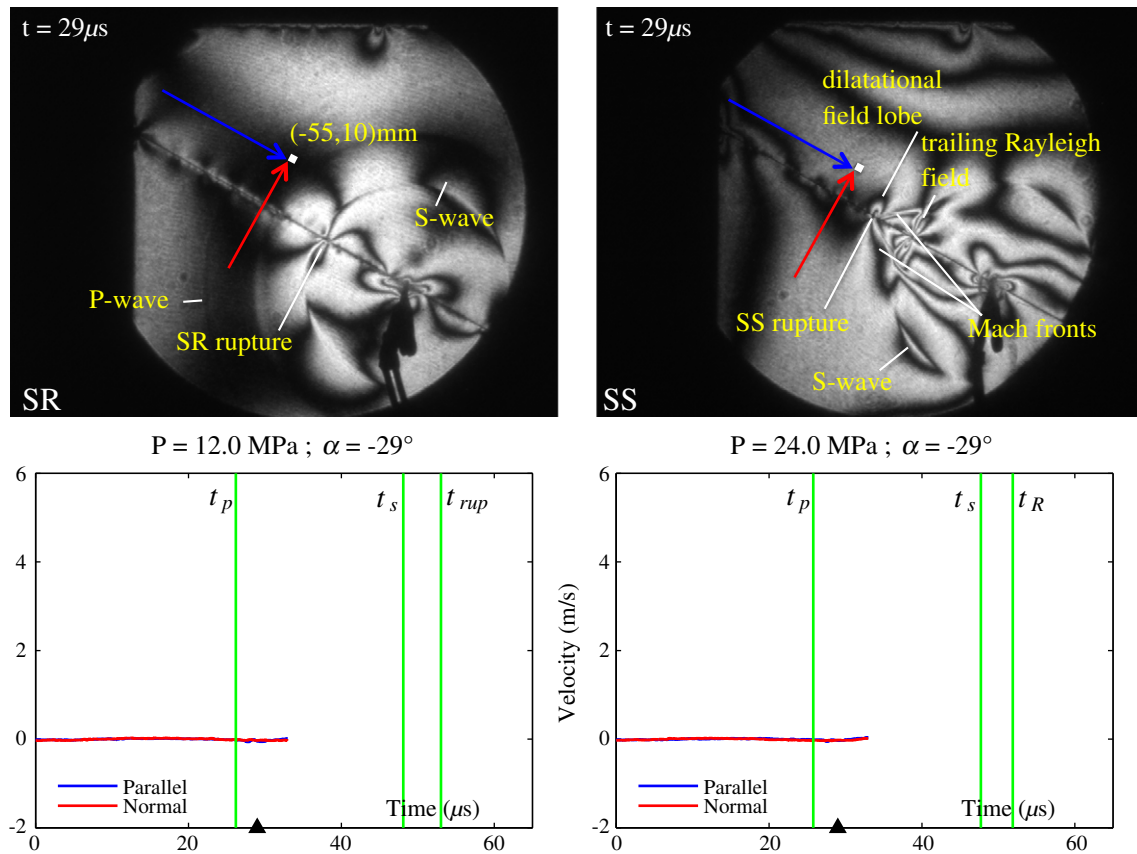Fig. 18. Extensional side experiments: $(-55,10)$mm at $t = 21\mu s$.

Fig. 19. Extensional side experiments: $(-55,10)$mm at $t = 29\mu s$.

Estimates of the trailing Rayleigh front propagation speed were obtained by tracking the point where the fringe pattern intersects the fault and plotting the position of this feature with respect to time. Best fit slope estimates reveal that the trailing Rayleigh disturbance propagates at $V_{tR} = 1.14 mm/\mu s$ ($V_r = 0.881 C_s$), which is close to the theoretical estimate of Rayleigh wave speed in H-100. Corresponding particle velocity station records remain quiet up to this point in time.

The (SR) image in Fig. 19 reveals that the P-wave front has already crossed the particle velocity measurement station. There little evidence of its crossing in the particle velocity records, however, since the P-wave is nearly nodal at this location. The intermediate circular banded region situated between the P-wave and S-wave fronts is a photoelastic manifestation of the near field region. This effect has been independently confirmed by plotting contours of maximum shear stress in finite element models. The sub-Rayleigh rupture front is still clearly visible in the left had image as revealed by the looping dark fringe stemming from the fault, situated just behind the leading S-wave front. Analysis of the rupture front position across successive image frames reveals a rupture speed of $V_r = 1.13 mm/\mu s$ ($V_r = 0.873 C_s$). Corresponding particle velocity station records remain quiet up to this point in time.

Fig. 20, acquired at $t = 37 \mu s$ shows that the shear Mach front, in the (SS) image on the right, is still several millimeters shy of crossing the particle velocity measurement station at $(-55, 10) mm$. Measurement of the shear Mach angles, both above and below the fault reveal a SS rupture speed value of $V_r = 2.15 mm/\mu s$ ($V_r = 1.67 C_s$). Note in particular how the corresponding particle velocity traces reveal pronounced velocity perturbations beginning at the point labeled a_0, at a time well in advance of the shear Mach front arrival (recall that the particle velocity trace extends out to $4 \mu s$ beyond the image frame time). The feature is clearly captured within the FP record by the noted velocity swing between points labeled a_0 and a_2. The sharp velocity increase commencing at point a_0, leading to a pronounced

peak approaching $\dot{u}_1 \approx 2.1 m/s$ at the point labeled (a_1), is attributed to the passage of a purely dilatational field, which circulates about the rupture tip and extends well beyond the shear Mach front.

A corresponding feature in the FN trace is revealed by the negative velocity swing, which also starts at a_0 and passes through the inflection point labeled b_0 on its way down to a minima of $\dot{u}_{1_{min}} \approx -1.7 m/s$ at the point labeled b_1 (seen in the next image sequence).

Meanwhile, the left hand (SR) image in Fig. 20, reveals that the rupture tip is still approximately 18 mm away from the measurement station. Feeble changes in the sub-Rayleigh FP record during this same time span are linked to the near field effects out ahead of the S-wave front.

Fig. 21, acquired $t = 41 \mu s$, reveals the shear Mach front in the process of crossing the particle velocity measurement station at $(-55, 10) mm$. Measurement of the shear Mach angles, both above and below the fault reveal a SS rupture speed value of $V_r = 2.27 m/s$ ($V_r/C_s = 1.76$) indicating that the rupture has accelerated relative to its speed as measured from the previous image frame. The arrival of the shear Mach front corresponds to the sharp positive velocity increase from $a_2 \rightarrow A$ in the FP particle velocity record and from $b_1 \rightarrow B$ in the FN record. Note how each signal exhibits a positive velocity swing in accordance with the anticipated sense of motion along a shear Mach front corresponding to a right lateral rupture at this location. The fault parallel velocity record jumps from a minimum value of $1.388 m/s$ at point a_2 up to a peak value of $\dot{u}_{1_{max}} \approx 5.4 m/s$ at point A. The resulting velocity swing from $a_2 \rightarrow A$ is given by $|\dot{u}_{1_{max}} - \dot{u}_{1_{min}}| = 4.0 m/s$. The corresponding FN velocity jump induced by the arrival of the shear Mach front ranges from $\dot{u}_{2_{min}} \approx -1.7 m/s$ at b_1 up to $\dot{u}_{2_{min}} \approx 0.433 m/s$ at the point labeled B. The resulting FN velocity swing is then given by $|\dot{u}_{2_{max}} - \dot{u}_{2_{min}}| \approx 2.12 m/s$. The arrival of the supershear rupture at the measurement station is characterized by a FP velocity swing that dominates over the FN velocity swing as expected.
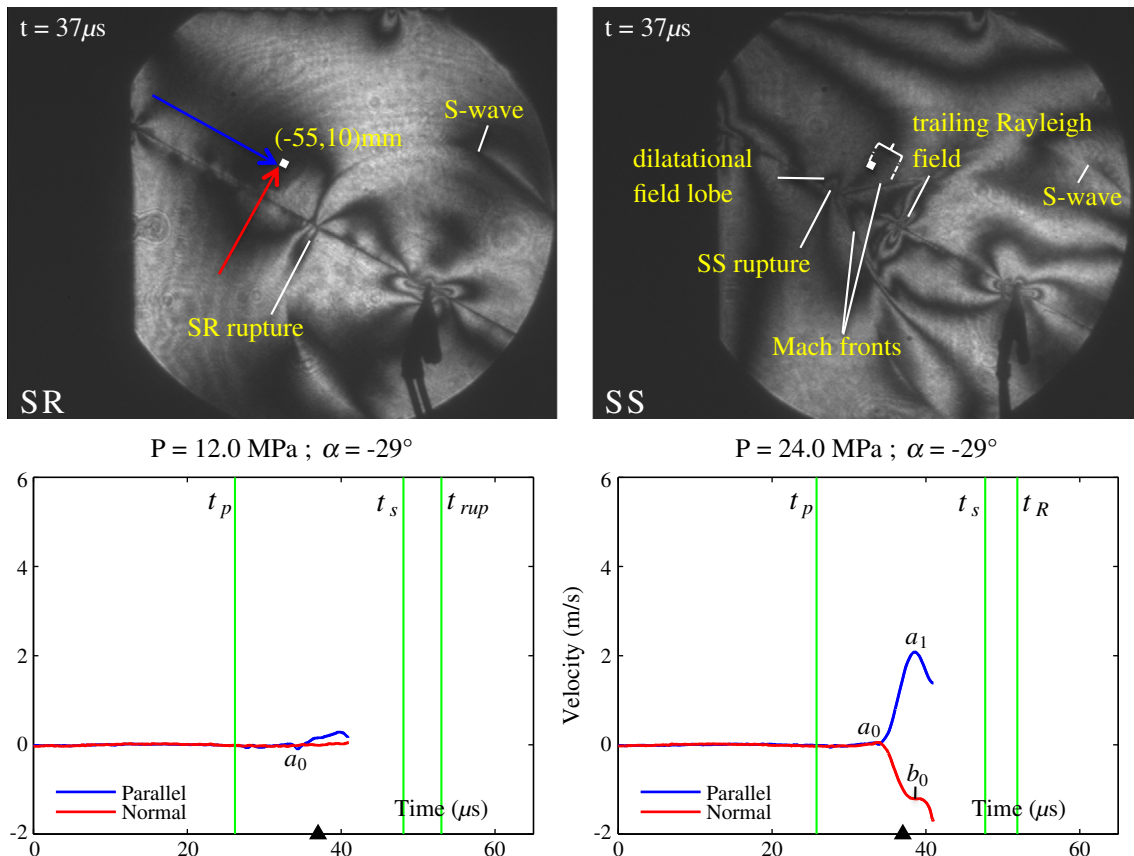

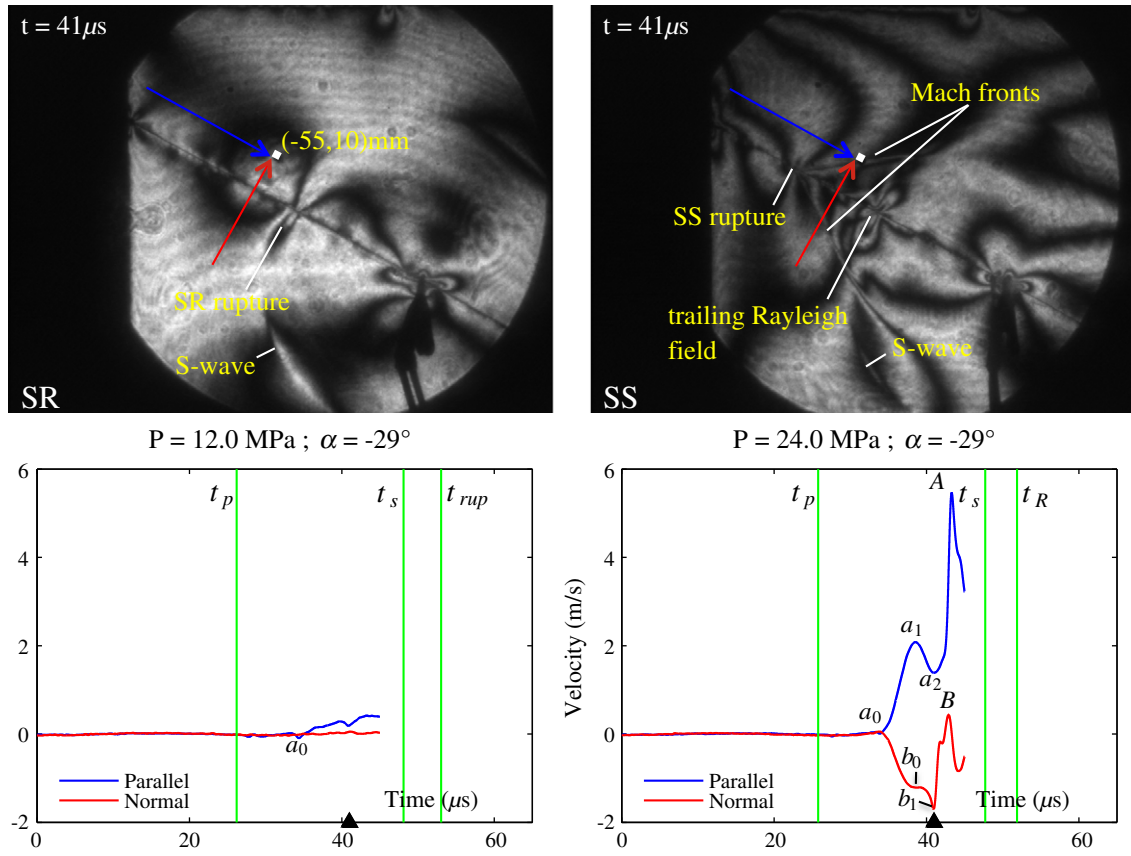**Fig. 20.** Extensional side experiments: $(-55,10)mm$ at $t = 37\mu s$.

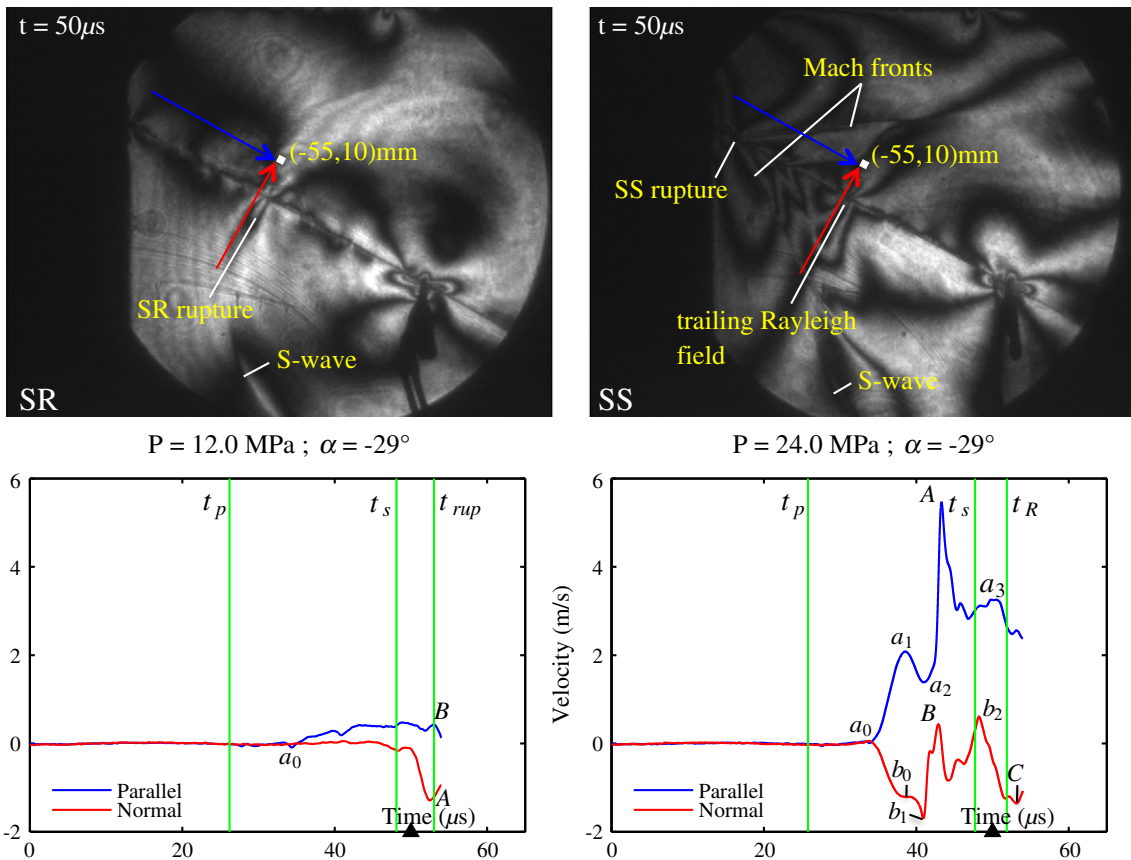**Fig. 21.** Extensional side experiments: $(-55,10)$mm at $t=41\mu s$.

Fig. 22. Extensional side experiments: $(-55,10)$mm at $t=50\mu s$.

The (SR) image on the left hand side in Fig. 21, acquired at $t = 41\mu s$, shows the advancing rupture front is still approximately 13 mm from the particle velocity station with the FN and FP particle velocity traces barely registering any changes other than a lazily climbing near field signal in the FP record, commencing at the point labeled a_0, associated with the near field region.

In Fig. 22, acquired at $t = 50\mu s$, the sub-Rayleigh rupture field is finally seen crossing the particle velocity station at $(-55, 10)mm$. The arrival of the sub-Rayleigh rupture at this location correlates very well with the pronounced velocity swing, commencing at $t = 50\mu s$, which extends down to a minimum value of $-1.29 m/s$ at the point labeled A. A negative FN velocity swing is consistent with the expected sense of particle motion induced by a right lateral sub-Rayleigh rupture measured on the extensional side of the fault. Note how there is only a very small change in the corresponding FP record at this time, labeled B.

The corresponding (SS) image in Fig. 22 captures the trailing Rayleigh disturbance sweeping the measurement station at $(-55, 10)mm$. This observation correlates very well with the pronounced drop from $b_2 \rightarrow C$ in the FN particle velocity record. Note the much smaller increase that occurred in the FP record during the same time interval, which peaked at the point labeled a_3. The noted velocity swings in the FN and FP records are perfectly consistent with the expected sense of motion induced by the passage of a right-lateral sub-Rayleigh rupture at a point on the extensional side of the fault. The green vertical line labeled t_R positioned at $t = 53\mu s$ denotes the anticipated arrival time of the trailing Rayleigh disturbance at $(-55, 0)mm$.

The final pair of images in Fig. 23, acquired at $t = 55\mu s$, show that the sub-Rayleigh rupture in the left hand (SR) image and the trailing Rayleigh disturbance in the right hand (SS) image have now both cleared the measurement station at $(-55, 10)mm$. The resulting velocity signatures associated with the passage of the sub-Rayleigh

rupture on the left, and the trailing Rayleigh disturbance on the right hand side are fully revealed. The dominance of the FN velocity swing over the FP velocity swing and the resulting sense of motion associated with the passage of each of these disturbances is in agreement with theoretical predictions as previously noted.

4.3. Laboratory earthquake based simulation of the $M_w7.9$ Denali, Alaska earthquake Pump station 10 ground motion records

4.3.1. Motivation for experimental investigations

We conclude by re-examining the 2002, $M_w7.9$ Denali fault earthquake and the remarkable set of ground motion records obtained at Pump Station 10 (PS10), located approximately 85 km east of the epicenter and 3 km north of the fault along the Alaska Pipeline (Eberhart-Phillips et al., 2003; Dunham and Archuleta, 2004; Ellsworth et al., 2004). Analysis of the PS10 records by Ellsworth et al. (2004) concluded that a supershear rupture swept by PS10 with a rupture speed approaching $V_r = 1.5C_s$. Synthetic ground motion curves captured the leading pulses featured in the FN, FP, and vertical ground motion records but were unable to replicate the prominent velocity fluctuations contained in the FN record that followed the primary rupture.

Dunham and Archuleta (2004) attributed these fluctuations to unsteady processes resulting from the sub-Rayleigh to supershear transition and followed with a dynamic model, which featured a slip weakening friction law and healing mechanism. Synthetic ground motion records replicated the leading supershear pulses and also captured a trailing Rayleigh disturbance propagating at the Rayleigh wave speed in the wake of the primary rupture. Emphasis was placed on matching the width of the supershear rupture pulses (labeled A and B) at the expense of truncating the width of the trailing Rayleigh disturbance. The fact that the synthetic curves fail to match up as well
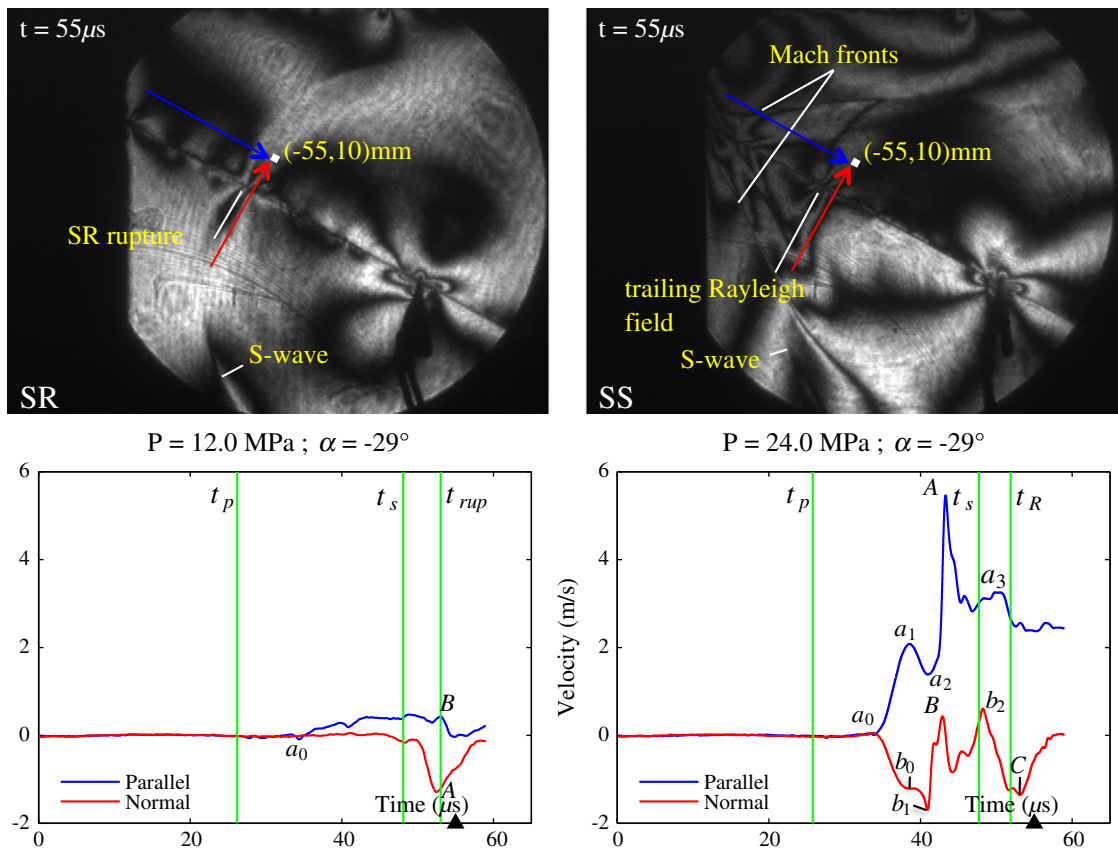

Fig. 23. Extensional side experiments: $(-55,10)mm$ at $t = 55\mu s$.

with trailing Rayleigh disturbance portion in the FN record was attributed to complex frictional faulting mechanisms not captured by the assumed frictional law.

The black curves in Fig. 24, reproduced here from Dunham and Archuleta (2004), represent the filtered Pump Station 10 ground motion records while the superimposed red curves correspond to synthetic ground motion predictions from the dynamic rupture model. The most obvious and striking feature of the PS10 ground motion records is the FP velocity pulse (labeled A in the figure) which is approximately $1.5\times$ greater in magnitude than the corresponding FN velocity pulse (labeled B). The second unique feature contained in these records corresponds to the set of pronounced velocity swings between points labeled C and D in the FN record, corresponding to the passage of a trailing Rayleigh disturbance arriving at the tail end of the supershear pulse. Note as well how this same feature is also revealed by the slip velocity color plot in Fig. 24b. Emphasis was placed on matching the width of the supershear rupture pulses (labeled A and emphB) at the expense of truncating the width of the trailing Rayleigh disturbance.

Motivated by the dynamic simulation and numerically based interpretations of these records, an attempt was made to replicate the Denali ground motion signatures using the laboratory earthquake arrangement. The experiments featured a left (west) to right(east) propagating rupture resulting from a right lateral strike slip of the model Homalite test specimen with particle velocity data collected at a near-field station situated just above (north of) the fault in order to simulate the PS10 scenario. Both sub-Rayleigh and supershear laboratory earthquake experiments were conducted using the "Denali PS10" configuration in order to compare and contrast the resulting particle velocity signatures. Sub-Rayleigh rupture experiments were conducted using a static pressure of $P = 5.4MPa$ while supershear experiments were conducted with a static pressure of $P = 24.1MPa$. The experiments featured a right-lateral rupture propagating left (west) to right (east) along an H-100 frictional fault. Continuous FN and FP Particle velocity records were collected at $(40, 2)mm$, thus mimicking the PS10 location situated on the north (compressional) side of the Denali fault. Synchronized photoelastic images were used

to visually track the location of the rupture front and other propagating field disturbances.

4.3.2. Analysis of photoelastic image sequence and particle velocity traces

Experimental results, as revealed by heterodyne interferometer particle velocity measurements and synchronized high speed imaging of photoelastic fringe patterns, are summarized below.

Fig. 25, acquired at $t = 18\mu s$, reveals a sub-Rayleigh (SR) in the left hand image and a supershear rupture (SS) in the right hand image both shown propagating toward the particle velocity measurement station situated at $(40, 2)mm$. The green vertical line segments labeled (t_p) at $t = 20.1\mu s$ and (t_s) at $t = 36\mu s$ correspond to the anticipated arrival times of the leading P-wave and S-wave fronts at $(40, 2)mm$. Note that $t = 0$ corresponds to the instrumentation trigger time and that a rupture nucleation delay time of $\Delta t = 4.78\mu s$ must be factored in order to reconcile the P-wave and S-wave arrival times at the measurement station. Circular P-wave fronts visible in both images are both just shy of the measurement station located at $(40, 2)mm$.

Fig. 26, acquired at $t = 21\mu s$, reveals that the leading circular P-wave fronts, which are still visible in each image, have both just crossed the measurement stations at $(40, 2)mm$. The supershear rupture tip in the right hand image is clearly visible in the image at the apex of the Mach cone. The sharp increase in the FP particle component and the corresponding smaller, yet equally sharp drop, in the FN component, commencing at the points labeled a_0 and b_0 in the supershear particle velocity traces, are attributed to the leading dilatational field, which swept the station prior to the arrival of the shear Mach front.

Close inspection of the supershear image in Fig. 27, acquired at $t = 25\mu s$, reveals the shear Mach crossing the lower right corner of the retro-reflective marker situated at $(40, 2)mm$. An instantaneous rupture speed $V_r = 2.15mm/us$ corresponding to $V_r/C_s = 1.67$ was obtained from this image frame by taking the average of the measured Mach angles to either side of the fault.

The FP and FN particle velocity records, which extend out to $t = 29\mu s$, reveal a pronounced velocity swing induced by the leading dilatational field, which extends from a_0 to a_2 in the FP record and from b_0 to B in the FN record. The contribution from the leading dilatational field is rather pronounced at this location due to its close proximity to the fault. The second sharp rise in the FP record commencing at point a_2 and rising to a maximum of $4.4m/s$ at point A along with the sudden drop ranging from B to b_2 in the FN trace during the same time interval correspond to the passage of the shear Mach front. Note how the FP velocity swing associated with the passage of the shear Mach front clearly dominates over the corresponding FN velocity swing as expected. Moreover, a positive jump in the FP signal accompanied by a negative change in the FN signal is consistent with the expected sense of motion along the shear Mach front at this location. Note as well how the resulting sense of particle motion in the current supershear experiment contrasts with the particle velocity measurements obtained at $(-55, 10)mm$ in the previous experiment, corresponding to a location on the extensional side of the fault, in which case which both motion components exhibited a positive rise in response to passage of the shear Mach front. The corresponding particle velocity traces in the sub-Rayleigh experiment remain relatively quiet during this time, apart from weak oscillations exhibited by the FP component, which are attributed to near field effects.

Fig. 28, acquired at $t = 37\mu s$, reveals that the S-wave front in the (SR) image on the left has just crossed the particle velocity measurement station. The accompanying particle velocity traces, which extend out to $t = 41\mu s$, reveal a sharp increase in both the FP and FN motion components commensurate with the arrival of the sub-Rayleigh rupture. Note how the particle velocity signature is characterized by a FN velocity swing, which clearly dominates the corresponding FP velocity swing as expected.
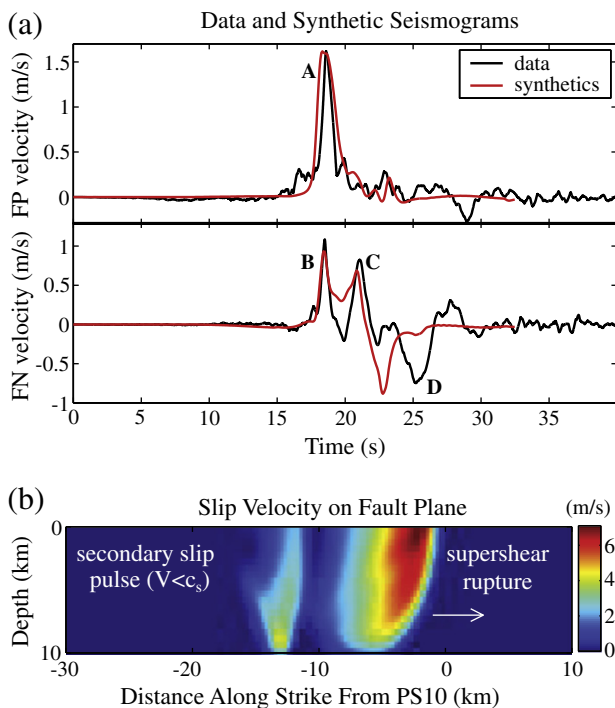

Fig. 24. Ground motion records captured at Pump Station 10 during M_w 7.9 Denali, Alaska earthquake on November 3, 2002. (Dunham and Archuleta, 2004).
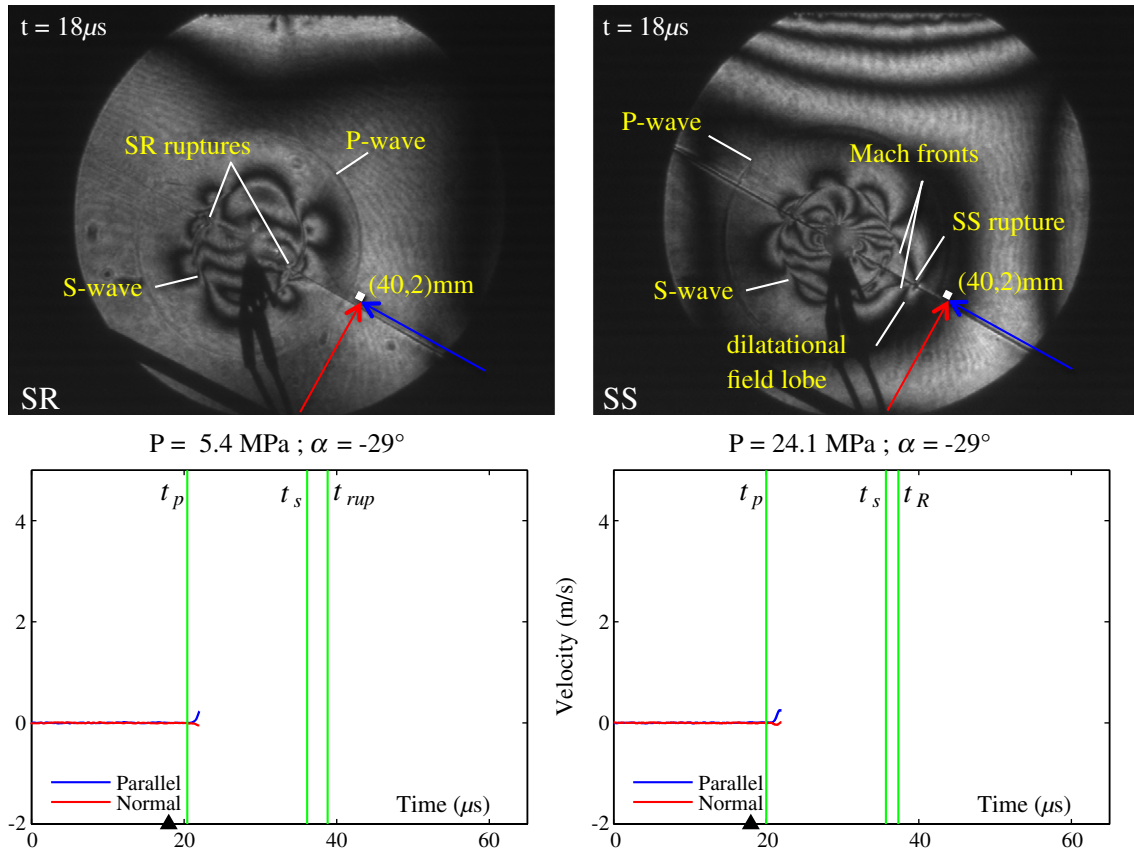
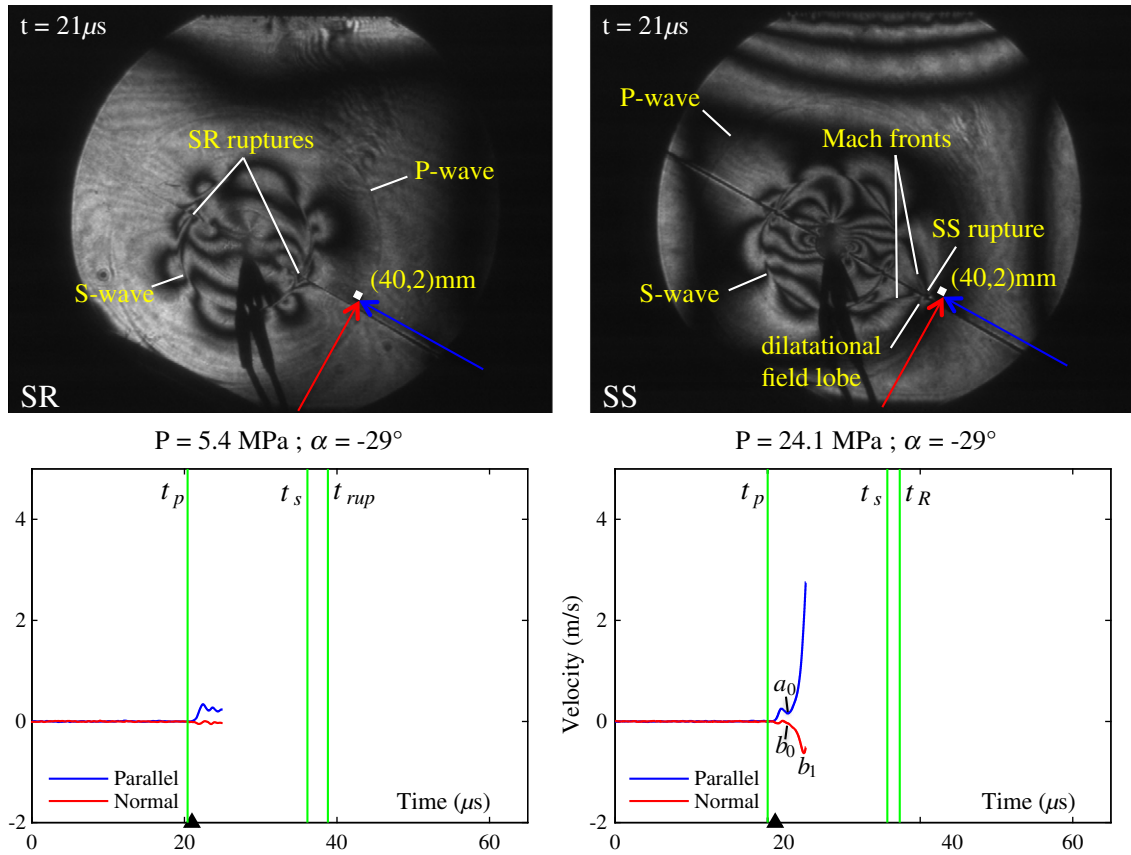Fig. 25. Compressional side experiments: (40,2)mm at $t = 18\mu s$.

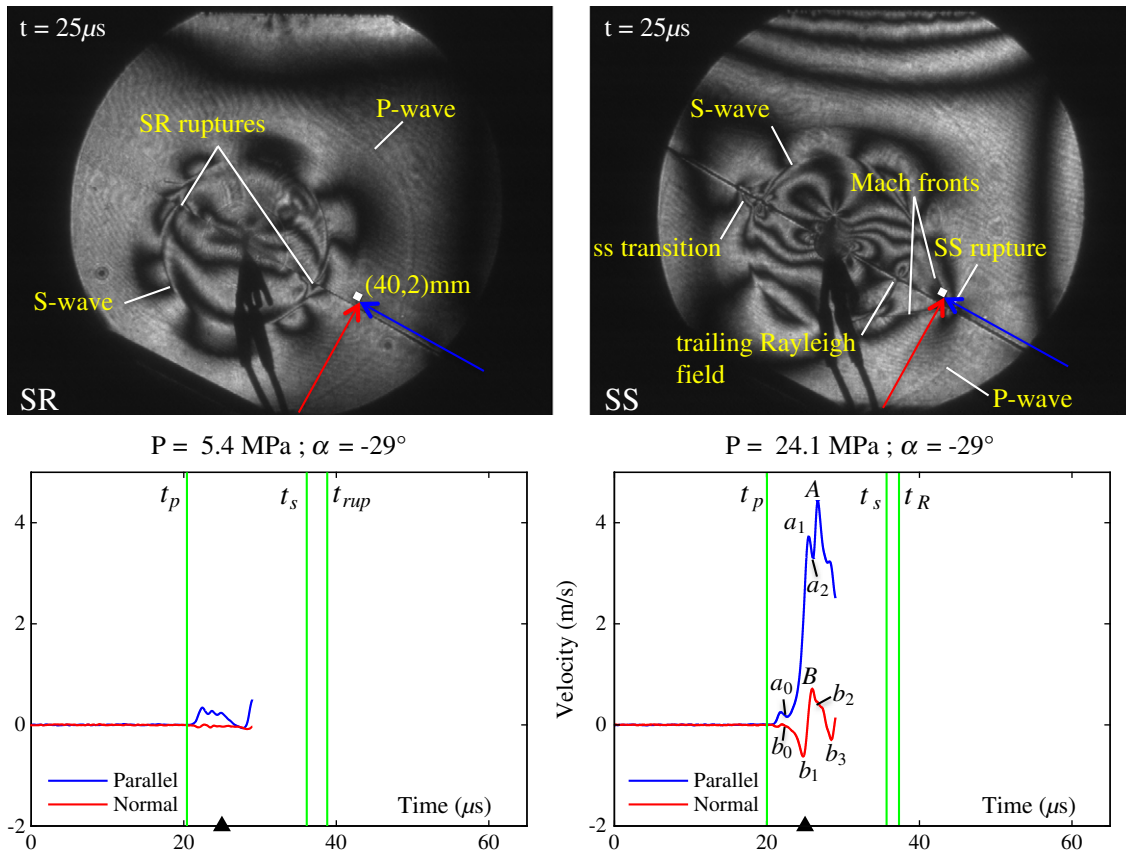Fig. 26. Compressional side experiments: (40,2)mm at $t = 21\mu s$.

Fig. 27. Compressional side experiments: (40,2)mm at $t = 25\mu s$.

The SS particle velocity traces that accompany the right hand image in Fig. 28 exhibit two perplexing velocity undulations, following the arrival of the shear Mach front, one of which commences at the point a_3 and peaks at A' in the FP record and the second which commences at b_3 and peaks at B' in the FN record. The timing of these pronounced velocity swings is not fully understood at this time. One possibility is that they are due to reflections through the thickness of the specimen. A simple isochrone analysis of a vertical rupture front (saturating the 9.55mm thickness of the specimen) propagating at constant speed does indeed reveal that these peaks at the particular station approximately correspond to information arriving from the bottom extent of the slipping region.

The (SS) image on the right hand side in Fig. 28 reveals a pair of looping fringes above and below the fault, in the wake of the shear Mach front, corresponding to the trailing Rayleigh disturbance. Close examination of the image reveals that the dark fringe loop situated above the fault has just crossed the lower right corner of the retroreflective marker at (40,2)mm where the FN and FP beams are focused. The trailing Rayleigh field center-of-symmetry, currently located at approximately (38,0)mm, is projected to cross the measurement station at $t = 38.7\mu s$ as denoted by the green vertical line labeled t_R. The sudden climb in the FN record, commencing at the point labeled b_4 and leading up to the peak at the point labeled hC, correlates with the arrival of the trailing Rayleigh disturbance at (40,2)mm. Note as well the corresponding rise in the FP signal, commencing at the point b_4, that was also registered during this same time period albeit to a lesser degree.

The final pair of images in Fig. 29, acquired at $t = 50\mu s$, reveal that the sub-Rayleigh rupture in the (SR) image and trailing Rayleigh field in the (SS) image have fully cleared the measurement station in each respective experiment. The resulting particle velocity traces, which extend out to $t = 54\mu s$, are free of any corrupting effects from wave reflections arriving from the specimen boundaries and reveal the particle velocity histories for each experiment. In the case of the sub-Rayleigh rupture, a dominant FN pulse is revealed with a prominent peak labeled A in the figure.

The velocity swing in the corresponding supershear FN record, which commences at point b_4, peaks at the point labeled C and extends down to point D, represents the defining ground motion signature resulting from the passage of the trailing Rayleigh disturbance. The corresponding FP velocity component exhibits a sharp increase starting at the point labeled a_4 up to a nearly constant value $\dot{u}_1 \approx 2.5 m/s$ (noted by point a_5), before dropping down to a nearly constant value $\dot{u}_1 \approx 2 m/s$ for the reminder of the pulse period. Both the sense of motion and dominance of the FN velocity swing over the FP velocity swing are consistent with the theoretical signatures of a rupture propagating at the Rayleigh wave speed. Last, but not the least, note that the FP trace reveals a crack like supershear rupture by virtue of the fact that the FP trace settles down to a nonzero value well after the primary rupture and trailing Rayleigh disturbance have passed. The experiment was thus characterized by a sub-Rayleigh crack, as previously noted, which transitioned to a supershear crack.

The crack-like signature obtained in the sub-Rayleigh and supershear experiments is consistent with previous experiments, which demonstrate how dynamic shear ruptures on interfaces that are prestressed in compression and in shear systematically vary from crack-like to pulse-like in accordance with the non-dimensional shear prestress or absolute stress levels (Lu et al., 2007, 2010). Experimental results are consistent with the theory of pulse-like and crack-like shear ruptures on velocity weakening interfaces (Zheng and Rice, 1998; Samudrala et al., 2002a). We acknowledge that while the PS 10 record shows a pulse-like rupture our experiments resulted in a crack-like rupture. The aim of our work here was not to reproduce the complete PS 10 record but to correlate ground motion signatures of laboratory and natural earthquakes associated with a supershear
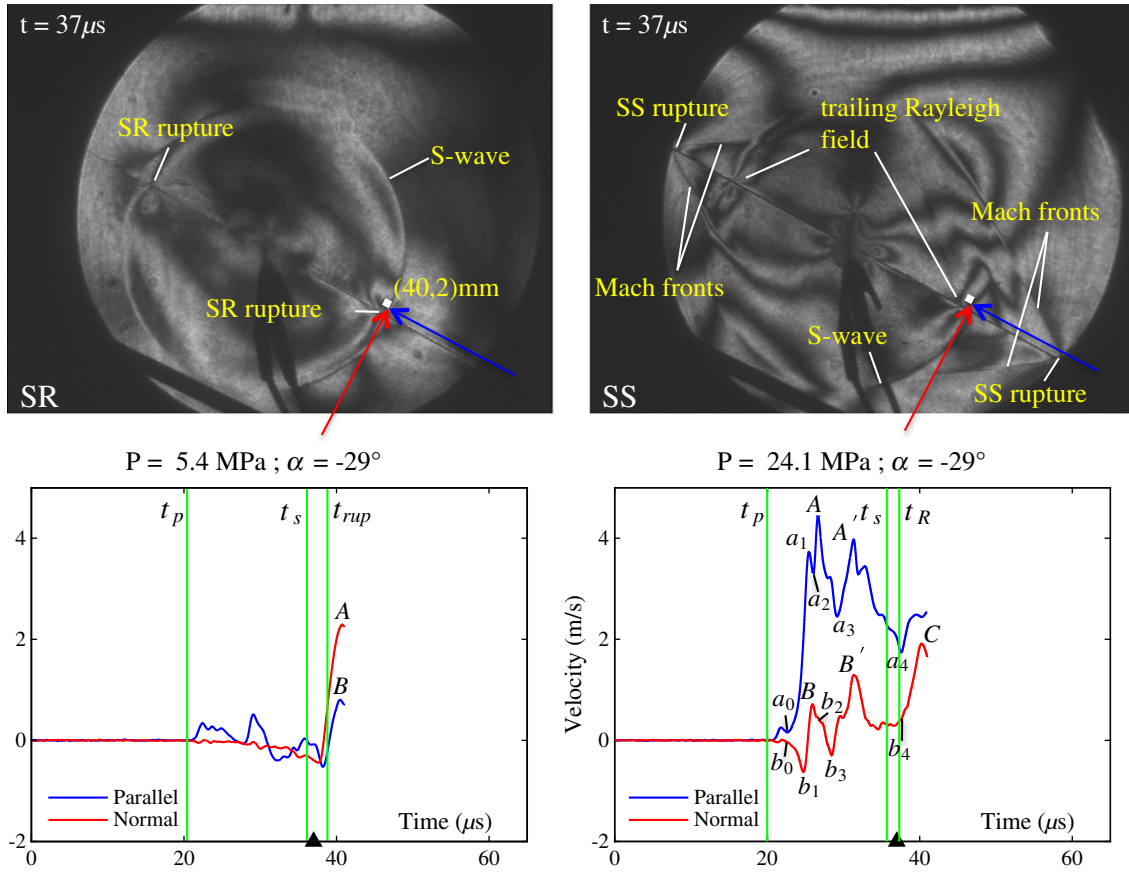
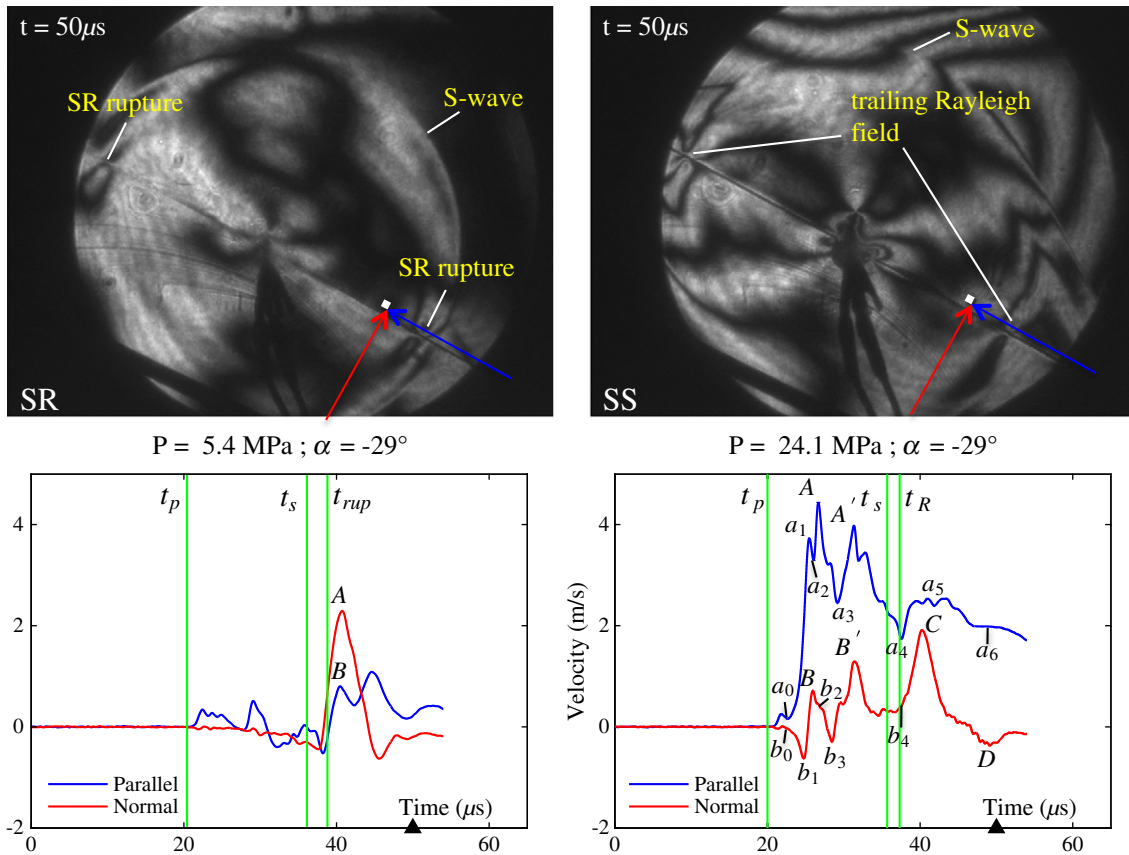**Fig. 28.** Compressional side experiments: (40,2)mm at $t = 37\mu s$.

Fig. 29. Compressional side experiments: (40,2)mm at $t = 50\mu s$.

rupture. Apart from the secondary peaks labeled A' and B', likely attributed to 3-D effects, and the fact that a crack-like instead of a pulse-like rupture resulted in the supeshear experiment, the resulting particle velocity records clearly bear amuch stronger resemblance to the Pump station 10 records than do the records obtained from the sub-Rayleigh experiment.

The first point to note upon comparing the supershear experimental records with the actual PS10 ground motion records is how the sign of the prominent velocity swings in the corresponding portions of the FP and FN records are in agreement. This observation is consistent with the choice of a measurement station on the compressional side of the fault located to the right (east) of the nucleation site and above (north) of the fault for a right-lateral rupture.

Next, note the dominance of the FP component over the FN component, as expected, during times corresponding to the arrival of the dilatational precursor and the shear Mach front in the experimental record. The tail end of the dilatational field portion of the FP and FN particle velocity records and the arrival of the shear Mach front in each of these traces is marked by sharp glitches at points labeled a_2 in the FP record and B in the FN record thus implying that the portion of the records associated with the passage of the shear Mach front is from $a_2 \rightarrow A$ in the FP record and from $B \rightarrow b_2$ in the FN record. The sense of particle motion along the shear Mach front is consistent with the expected sense of motion along a shear Mach front for a right-lateral rupture propagating in the stable rupture speed regime.

There is no apparent distinction between the dilatational field and the shear Mach front contributions in the corresponding PS10 ground motion records. This could be attributed to the fact that the PS10 station was closer to the fault in a relative scaling sense than the experimental station located at $(40,2)mm$. Another reason could be that, while the experimental records were due to an essentially 2D rupture, the Denali event was 3D by nature. This point is bolstered by the results of the dynamic 3D calculations done by Dunham and Archuleta (2004) which do not reveal such a clear distinction between the leading dilatational field and the shear Mach front.

The supershear image frame in Fig. 28, acquired at $t = 37\mu s$, links the arrival of the trailing Rayleigh disturbance at the particle velocity measurement station to the pronounced velocity swing registered in the FN record between the points labeled C and D. As noted by Dunham and Archuleta (2004) the almost antisymmetric nature of this part of the record at PS 10 reveals that the trailing Rayleigh disturbance was pulse-like. Since we have a crack-like rupture the trailing Rayleigh disturbance fails to heal completely and hence the record is not as antisymmetric. Nevertheless, the result captures the same general features and sense of motion observed in the corresponding portion of the PS10 FN ground motion record, and provides experimental confirmation that this portion of the record can be attributed to the passage of a trailing Rayleigh disturbance.

5. Summary and Conclusions

We have identified the unique near field signatures in the ground velocity records for both sub-Rayleigh and supershear ruptures. Collating some of the previous work done on these ruptures we have presented a rigorous theoretical and numerical argument regarding these signatures. For example, we clearly show that the dominance of the fault parallel velocity component in the rupture speed regime ($\sqrt{2}C_s < V_r \leq C_p$) is a fundamental nature of ruptures whose velocities exceed the S-wave speed of the material.

We have experimentally validated that a rupture traveling at supershear speeds has the following analytically predicted signatures.

- A dilatational precursor, dominant in the fault parallel component, that arrives in the ground motion records prior to the arrival of the Mach front.

- Dominance of the fault parallel component over the fault normal component in the supershear speed regime ($\sqrt{2}C_s < V_r \leq C_p$).
- Trailing Rayleigh rupture behind the main rupture tip with a dominant fault normal component. This produces a ground shaking signature qualitatively similar to a sub-Rayleigh rupture.

We have also conducted experiments to replicate some extent of the 2002 Denali event and have identified two of the three signatures, listed above, both in the experimental and natural earthquake (Pump Station 10) records thus experimentally validating the argument of (Dunham and Archuleta, 2004) that part of the Denali rupture did indeed travel at supershear speeds. The direct practical consequence of the above observations are that a near field station will first experience the primary Fault Parallel (FP) shaking due to the shock structure and will subsequently feel a primary Fault Normal (FN) shaking of the trailing Rayleigh disturbance. The timing between these two occurrences will depend on the location of the near field station relative to the point of sub-Rayleigh to supershear transition. Structures located near a fault hosting such a transition will effectively experience two separate, closely-timed earthquake events characterized by different forms of ground shaking.

References

Aagaard, B.T., Heaton, T.H., 2004. Near-source ground motions from simulations of sustained intersonic and supersonic fault ruptures. Bull. Seismol. Soc. Am. 94, 2064–2078.
Aki, K., Richards, P.G., 2002. Quantitative Seismology. University Science Books.
Andrews, D.J., 1976. Rupture velocity of plane strain shear cracks. J. Geophys. Res. 81 (B32), 5679–5689.
Archuleta, R.J., 1984. A faulting model for the 1979 Imperial Valley earthquake. J. Geophys. Res. 89 (B6), 4559–4586.
Barenblatt, G.I., 1962. The mathematical theory of equilibrium cracks in brittle fracture. Adv. Appl. Mech. 7 (2), 55–129.
Bhat, H.S., Dmowska, R., King, G.C.P., Klinger, Y., Rice, J.R., 2007. Off-fault damage patterns due to supershear ruptures with application to the 2001 M_w 8.1 Kokoxili (Kunlun) Tibet earthquake. J. Geophys. Res. B06301. doi:10.1029/ 2006JB004425.
Bouchon, M., Karabulut, H., 2008. The aftershock signature of supershear earthquakes. Science 320 (5881), 1323.
Bouchon, M., Vallee, M., 2003. Observation of long supershear rupture during the magnitude 8.1 Kunlunshan earthquake. Science 301, 824–826.
Bouchon, M., Bouin, M.P., Karabulut, H., Toksoz, M.N., Dietrich, M., Rosakis, A.J., 2001. How fast is rupture during an earthquake? New insights from the 1999 Turkey earthquakes. Geophys. Res. Lett. 28, 2723–2726.
Bouchon, M., Toksoz, M.N., Karabulut, H., Bouin, M.P., Dietrich, M., Aktar, M., Edie, M., 2002. Space and time evolution of rupture and faulting during the 1999 Izmit (Turkey) earthquake. Bull. Seismol. Soc. Am. 92, 256–266.
Bouin, M., Bouchon, M., Karabulut, H., Aktar, M., 2004. Rupture process of the 1999 November 12 Duzce (Turkey) earthquake deduced from strong motion and global positioning system measurements. Geophys. J. Int. 159, 207–211.
Broberg, K.B., 1978. On transient sliding motion. Geophys. J. Roy. Astr. Soc. 52, 397–432.
Broberg, K.B., 1989. The near-tip field at high crack velocities. Int. J. Fract. 39 (1), 1–13.
Broberg, K.B., 1994. Intersonic bilateral slip. Geophys. J. Int. 119, 706–714.
Broberg, K.B., 1999. Cracks and Fracture. Academic Press.
Burridge, R., 1973. Admissible speeds for plane-strain self-similar shear cracks with friction but lacking cohesion. Geophys. J. Roy. Astron. Soc. 35, 439–455.
Burridge, R., Conn, G., Freund, L.B., 1979. Stability of a rapid mode-II shear crack with finite cohesive traction. J. Geophys. Res. 84, 2210–2222.
Coker, D., Lykotrafitis, G., Needleman, A., Rosakis, A.J., 2005. Frictional sliding modes along an interface between identical elastic plates subject to shear impact loading. J. Mech. Phys. Solids 53, 884–922.
Dally, J., Riley, W., 2005. Experimental Stress Analysis, 4th ed. College House Enterprises, LLC.
Das, S., 2007. The need to study speed. Science 317 (5840), 905–906.
Dugdale, D., 1960. Yielding of steel sheets containing slits. J. Mech. Phys. Solids 8, 66–75.
Dunham, E.M., Archuleta, R.J., 2004. Evidence for a supershear transient during the 2002 Denali fault earthquake. Bull. Seismol. Soc. Am 94, S256–S268.
Dunham, E.M., Archuleta, R.J., 2005. Near-source ground motion from steady state dynamic rupture pulses. Geophys. Res. Lett. 32.

Dunham, E.M., Bhat, H.S., 2008. Attenuation of radiated ground motion and stresses from three-dimensional supershear ruptures. J. Geophys. Res. 113 (B08319). doi:10.1029/2007JB005182.

Eberhart-Phillips, D., et al., 2003. The 2002 Denali fault earthquake, Alaska: A large magnitude, slip-partitioned event. Science 300, 1113–1118.

Ellsworth, W., Chiaraluce, L., 2009. Supershear during nucleation of the 2009 M 6.3 L'Aquila, Italy Earthquake. Fall Meet. Suppl., Abstract U13B–0068: Eos Trans. AGU, 90(52).

Ellsworth, W.L., Celebi, M., Evans, J.R., Jensen, E.G., Nyman, D.J., Spudich, P., 2004. Processing and modeling of the pump station 10 record from the November 3, 2002, Denali fault, Alaska earthquake. Proceedings, 11th Intern. Conf. Soil Dynam. Earthq. Eng, 1, pp. 471–477.

Freund, L.B., 1979. Mechanics of dynamic shear crack-propagation. J. Geophys. Res. 84 (B5), 2199–2209.

Freund, L.B., 1990. Dynamic Fracture Mechanics. Cambridge University Press, Cambridge.

Gao, H., Huang, Y., Gumbsch, P., Rosakis, A., 1999. On radiation-free transonic motion of cracks and dislocations. J. Mech. Phys. Solids 47, 1941–1961.

Ida, Y., 1972. Cohesive force across tip of a longitudinal-shear crack and Griffiths specific surface-energy. J. Geophys. Res. 77, 3796–3805.

Kobayashi, A. (Ed.), 1993. Handbook of Experimantal Mechanics. Wiley.

Kostrov, B.V., 1966. Unsteady propagation of longitudinal shear cracks. J. Appl. Math. Mech. 30, 1241–1248.

Kostrov, B.V., Nikitin, L.V., 1970. Some general problems of mechanics of brittle fracture. Arch. Mech. 22 (6), 749–776.

Kostrov, B., Nikitin, L.V., Flitman, L.M., 1969. The mechanics of brittle fracture. Izv. Akad. Nauk SSSR, Mekh. Tverd. Tela, 3, pp. 112–125.

Lambros, J., Rosakis, A.J., 1995. Shear dominated transonic interfacial crack-growth in a bimaterial. 1. Experimental-observations. J. Mech. Phys. Solids 43, 169–188.

Liu, C., Huang, Y., Rosakis, A.J., 1995. Shear dominated transonic interfacial crack-growth in a bimaterial. 2. Asymptotic fields and favorable velocity regimes. J. Mech. Phys. Solids 43, 189–206.

Lu, X., Lapusta, N., Rosakis, A.J., 2007. Pulse-like and crack-like ruptures in experiments mimicking crustal earthquakes. Proc. Natl Acad. Sci. USA 104 (48), 18,931–18,936.

Lu, X., Lapusta, N., Rosakis, A.J., 2009. Analysis of supershear transition regimes in rupture experiments: the effect of nucleation conditions and friction parameters. Geophys. J. Int. 177 (2), 717–732.

Lu, X., Lapusta, N., Rosakis, A., 2010. Pulse-like and crack-like dynamic shear ruptures on frictional interfaces: experimental evidence, numerical modeling, and implications. Int. J. Fract. 1–13. doi:10.1007/s10704-010-9479-4.

Lykotrafitis, G., Rosakis, A.J., 2006. Dynamic sliding of frictionally held bimaterial interfaces subjected to impact shear loading. Proc. R. Soc. A-Math. Phys. Eng. Sci. 462, 2997–3026.

Lykotrafitis, G., Rosakis, A., Ravichandran, G., 2006a. Self-healing pulse-like shear ruptures in the laboratory. Science 313 (5794), 1765–1768.

Lykotrafitis, G., Rosakis, A.J., Ravichandran, G., 2006b. Particle velocimetry and photoelasticity applied to the study of dynamic sliding along frictionally-held bimaterial interfaces: techniques and feasibility. Exp. Mech. 46, 205–216.

Madariaga, R., 1977. High-frequency radiation from crack (stress drop) models of earthquake faulting. Geophys. J. Roy. Astron. Soc. 51, 625–651.

Muskhelishvili, N.I., 1953. Singular Integral Equations: Boundary Problems of Function Theory and their Application to Mathematical Physics. In: Radok, J.R.M., Nordoff, P., Groningen (Eds.), Translation from Russian.

Ohnaka, M., 2003. A constitutive scaling law and a unified comprehension for frictional a constitutive scaling law and a unified comprehension for frictional slip failure, shear fracture of intact rock, and earthquake rupture. J. Geophys. Res. 108 (B2).

Palmer, A.C., Rice, J.R., 1973. Growth of slip surfaces in progressive failure of over-consolidated clay. Proc. R. Soc. London. Ser. A-Math. Phys. Eng. Sci. 332, 527–548.

Rice, J.R., Sammis, C.G., Parsons, R., 2005. Off-fault secondary failure induced by a dynamic slip pulse. Bull. Seismol. Soc. Am. 95 (1), 109–134.

Robinson, D.P., Brough, C., Das, S., 2006. The M_w 7.8, 2001 Kunlunshan earthquake: extreme rupture speed variability and effect of fault geometry. J. Geophys. Res. 111 (B8).

Rosakis, A.J., 2002. Intersonic shear cracks and fault ruptures. Adv. Phys. 51, 1189–1257.

Rosakis, A.J., Samudrala, O., Singh, R.P., Shukla, A., 1998. Intersonic crack propagation in bimaterial systems. J. Mech. Phys. Solids 46, 1789–1813.

Rosakis, A.J., Samudrala, O., Coker, D., 1999. Cracks faster than the shear wave speed. Science 284, 1337–1340.

Rosakis, A.J., Xia, K.W., Lykotrafitis, G., Kanamori, H., 2007. In: Kanamori, H. (Ed.), Dynamic shear rupture in frictional interfaces: speeds, directionality and modes: Treatise in Geophysics, vol. 4, pp. 153–192.

Samudrala, O., Huang, Y., Rosakis, A.J., 2002a. Subsonic and intersonic shear rupture of weak planes with a velocity weakening cohesive zone. J. Geophys. Res. 107 (B8). doi:10.1029/2001JB000460.

Samudrala, O., Huang, Y., Rosakis, A.J., 2002b. Subsonic and intersonic mode II crack propagation with a rate-dependent cohesive zone. J. Mech. Phys. Solids 50, 1231–1268.

Song, S.G., Beroza, G., Segall, P., 2008. A unified source model for the 1906 San Francisco earthquake. Bull. Seismol. Soc. Am. 98 (2), 823–831.

Xia, K.W., Rosakis, A.J., Kanamori, H., 2004. Laboratory earthquakes: the sub-Rayleigh-to-supershear rupture transition. Science 303, 1859–1861.

Xia, K.W., Rosakis, A.J., Kanamori, H., 2005a. Supershear and sub-Rayleigh to supershear transition observed in laboratory earthquake experiments. Exp. Tech. 29, 63–66.

Xia, K.W., Rosakis, A.J., Kanamori, H., Rice, J.R., 2005b. Laboratory earthquakes along inhomogeneous faults: Directionality and supershear. Science 308, 681–684.

Zheng, G., Rice, J., 1998. Conditions under which velocity-weakening friction allows a self-healing versus a cracklike mode of rupture. Bull. Seismol. Soc. Am. 88 (6), 1466–1483.